

CHARACTERIZATION OF NON-LINEARIZED SPACECRAFT RELATIVE MOTION USING NONLINEAR NORMAL MODES

Eric A. Butcher

**University of Arizona
888 N Euclid Ave
Tucson, AZ 85719-4824**

20 Apr 2016

Final Report

APPROVED FOR PUBLIC RELEASE; DISTRIBUTION IS UNLIMITED.



**AIR FORCE RESEARCH LABORATORY
Space Vehicles Directorate
3550 Aberdeen Ave SE
AIR FORCE MATERIEL COMMAND
KIRTLAND AIR FORCE BASE, NM 87117-5776**

DTIC COPY

NOTICE AND SIGNATURE PAGE

Using Government drawings, specifications, or other data included in this document for any purpose other than Government procurement does not in any way obligate the U.S. Government. The fact that the Government formulated or supplied the drawings, specifications, or other data does not license the holder or any other person or corporation; or convey any rights or permission to manufacture, use, or sell any patented invention that may relate to them.

This report is the result of contracted fundamental research deemed exempt from public affairs security and policy review in accordance with SAF/AQR memorandum dated 10 Dec 08 and AFRL/CA policy clarification memorandum dated 16 Jan 09. This report is available to the general public, including foreign nationals. Copies may be obtained from the Defense Technical Information Center (DTIC) (<http://www.dtic.mil>).

AFRL-RV-PS-TR-2015-0182 HAS BEEN REVIEWED AND IS APPROVED FOR PUBLICATION IN ACCORDANCE WITH ASSIGNED DISTRIBUTION STATEMENT.

//SIGNED//

THOMAS LOVELL
Program Manager

//SIGNED//

PAUL HAUSGEN, Ph.D.
Technical Advisor, Spacecraft Component Technology

//SIGNED//

JOHN BEAUCHEMIN
Chief Engineer, Spacecraft Technology Division
Space Vehicles Directorate

This report is published in the interest of scientific and technical information exchange, and its publication does not constitute the Government's approval or disapproval of its ideas or findings.

Approved for public release; distribution is unlimited.

REPORT DOCUMENTATION PAGE				Form Approved OMB No. 0704-0188	
Public reporting burden for this collection of information is estimated to average 1 hour per response, including the time for reviewing instructions, searching existing data sources, gathering and maintaining the data needed, and completing and reviewing this collection of information. Send comments regarding this burden estimate or any other aspect of this collection of information, including suggestions for reducing this burden to Department of Defense, Washington Headquarters Services, Directorate for Information Operations and Reports (0704-0188), 1215 Jefferson Davis Highway, Suite 1204, Arlington, VA 22202-4302. Respondents should be aware that notwithstanding any other provision of law, no person shall be subject to any penalty for failing to comply with a collection of information if it does not display a currently valid OMB control number. PLEASE DO NOT RETURN YOUR FORM TO THE ABOVE ADDRESS.					
1. REPORT DATE (DD-MM-YY) 20-04-2016		2. REPORT TYPE Final Report		3. DATES COVERED (From - To) 3 Sep 2014 – 03 Mar 2016	
4. TITLE AND SUBTITLE Characterization of Non-Linearized Spacecraft Relative Motion using Nonlinear Normal Modes				5a. CONTRACT NUMBER FA9453-14-1-0350	
				5b. GRANT NUMBER	
				5c. PROGRAM ELEMENT NUMBER 62601F	
6. AUTHOR(S) Eric A. Butcher				5d. PROJECT NUMBER 8809	
				5e. TASK NUMBER PPM00018802	
				5f. WORK UNIT NUMBER EF122707	
7. PERFORMING ORGANIZATION NAME(S) AND ADDRESS(ES) University of Arizona 888 N Euclid Ave Tucson, AZ 85719-4824				8. PERFORMING ORGANIZATION REPORT NUMBER	
9. SPONSORING / MONITORING AGENCY NAME(S) AND ADDRESS(ES) Air Force Research Laboratory Space Vehicles Directorate 3550 Aberdeen Ave. SE Kirtland AFB, NM 87117-5776				10. SPONSOR/MONITOR'S ACRONYM(S) AFRL/RVSV	
				11. SPONSOR/MONITOR'S REPORT NUMBER(S) AFRL-RV-PS-TR-2015-0182	
12. DISTRIBUTION / AVAILABILITY STATEMENT Approved for public release; distribution is unlimited.					
13. SUPPLEMENTARY NOTES					
14. ABSTRACT Characterize the nonlinear dynamics for large amplitude relative motion in the Hill frame (or curvilinear frame) in terms of Nonlinear Normal Modes for the case of a circular chief orbit. Characterize the nonlinear dynamics for nonlinear translationalrotational coupling of relative motion in terms of Nonlinear Normal Modes. Characterize the nonlinear dynamics for an elliptic Keplerian chief orbit in terms of time periodic Nonlinear Normal Modes using the Liapunov-Floquet transformation. If time permits, investigate the relative navigation problem in the Nonlinear Normal Modes NNMs framework, using the strategies outlined above.					
15. SUBJECT TERMS Nonlinear Normal Modes; NNMs; Tschauner-Hempel-Lawden; THL; Relative Orbit Elements; ROEs; Linear Normal Modes; Degree-of-freedom Vibratory Systems; Liapunov-Floquet transformation; LFT					
16. SECURITY CLASSIFICATION OF:			17. LIMITATION OF ABSTRACT	18. NUMBER OF PAGES	19a. NAME OF RESPONSIBLE PERSON
a. REPORT	b. ABSTRACT	c. THIS PAGE			Thomas A. Lovell
Unclassified	Unclassified	Unclassified	Unlimited	50	19b. TELEPHONE NUMBER (include area code)

This page is intentionally left blank

TABLE OF CONTENTS

Section	Page
List of Figures	ii
List of Tables.....	iii
1.0 SUMMARY	1
2.0 INTRODUCTION.....	2
3.0 METHODS, ASSUMPTIONS, AND PROCEDURES.....	3
3.1 Dynamics of Relative Motion with Different Nonlinearities	3
3.2 Measurements.....	4
3.3 Analytical Observability Criteria for Nonlinear Systems	5
3.4 Numerical Observability Measure of Nonlinear Systems.....	6
4.0 OBSERVABILITY ANALYSIS FOR RELATIVE MOTION WITH LOS MEASUREMENTS	8
5.0 NUMERICAL RESULTS FOR OBSERVABILITY ANALYSIS OF RELATIVE MOTION.....	10
5.1 Results for Four Models with Different Nonlinearities	11
5.2 Effects of Nonlinearities on the Observability of Different Configurations	14
6.0 AMBIGUOUS ORBITS OF HCW MODEL WITH RANGE-ONLY MEASUREMENTS	18
6.1 Definition of Ambiguous Orbits.....	18
6.2 Mirror Ambiguous Orbits.....	21
6.3 Deformed Ambiguous Orbits	23
6.4 Existence of Deformed Ambiguous Orbits	27
6.5 Categorization of Ambiguous Relative Orbits	29
6.6 Numerical Results for Ambiguity Analysis.....	31
7.0 RESULTS AND DISCUSSION	35
8.0 CONCLUSIONS	38
REFERENCES	39
LIST OF SYMBOLS, ABBREVIATIONS, AND ACRONYMS.....	40

Approved for public release; distribution is unlimited.

LIST OF FIGURES

Figure	Page
Figure 1. Measurement Relationship in Chief's LVLH Frame	5
Figure 2. The True Relative Orbit in Chief's LVLH Frame with 3-D Projections	10
Figure 3. True and Estimated Orbits with Range-only Measurements	12
Figure 4. True and Estimated Orbits with Angles-only Measurements	13
Figure 5. Ratio Plots of OI and CN with Varying Inclination Difference	14
Figure 6. Ratio Plots of OI and CN with Varying Mean Anomaly Difference	15
Figure 7. Ratio Plots of OI and CN with Varying Eccentricity Difference	16
Figure 8. Plots of OI and CN for Different Orders of Nonlinearities (Range-only)	16
Figure 9. Plots of OI and CN for Different Orders of Nonlinearities (Angles-only)	17
Figure 10. Maximum Relative Distance in Three Directions with Increasing δi	17
Figure 11. First Case of Ambiguity Using HCW Based EKF	18
Figure 12. Second Case of Ambiguity Using HCW Based EKF	19
Figure 13. Third Case of Ambiguity Using HCW Based EKF	20
Figure 14. True Relative Orbit and Three Mirror Ambiguous Orbits	23
Figure 15. True Relative Orbit and Four Deformed Ambiguous Orbits	26
Figure 16. Three Polynomials and Corresponding Solutions	27
Figure 17. Cases of Transverse and Tangent Intersections for $h(K)$ and c	28
Figure 18. Illustration of Tangent Condition	29
Figure 19. Illustration of Offset y_{d0} and Slope s in $y - z$ Projection	30
Figure 20. Drifting True and Mirror Ambiguous Orbits in an EKF Simulation	31
Figure 21. Type (c) Mirror Ambiguous Orbit in an EKF Simulation	32
Figure 22. Type (e) Deformed Ambiguous Orbit in an EKF Simulation	33
Figure 23. Relative Orbits Resulting from Variation of Initial Conditions	34
Figure 24. Convergence of EKF Simulations for Small Relative Orbit Scenario	35
Figure 25. Convergence of EKF for Medium and Large Relative Orbit Scenarios	36
Figure 26. Convergence of EKF for HCW Model with Three Relative Orbit Scenarios	36
Figure 27. Convergence of EKF for Full Nonlinear Model with Three Scenarios	37

LIST OF TABLES

Table	Page
Table 1. Orbital Element Differences for Primary Simulation Case.....	10
Table 2. Performance of EKF Based on Range-only Measurements.....	11
Table 3. Performance of EKF Based on Angles-only Measurements.....	13
Table 4. Types of Mirror Ambiguous Orbits in Initial Cartesian Coordinates.....	22
Table 5. Initial Condition for True Relative Orbit	23
Table 6. Categorization of Ambiguous Orbits	30
Table 7. Orbital Element Differences for Drifting and Non-drifting Scenarios	32
Table 8. Orbital Element Differences for Three Simulation Scenarios	34

ACKNOWLEDGMENTS

This material is based on research sponsored by Air Force Research Laboratory under agreement number FA9453-15-1-0350. The U.S. Government is authorized to reproduce and distribute reprints for Governmental purposes notwithstanding any copyright notation thereon.

DISCLAIMER

The views and conclusions contained herein are those of the authors and should not be interpreted as necessarily representing the official policies or endorsements, either expressed or implied, of Air Force Research Laboratory or the U.S. Government.

1.0 SUMMARY

In this report, the effects of incorporating nonlinearities in sequential relative orbit estimation are studied for a chief spacecraft in a circular orbit, assuming either range-only or angles-only measurement of the deputy from the chief. The relative motion models can be categorized into four cases: first order Hill-Clohessy-Wiltshire (HCW) equation, second order, third order and full nonlinear. Observability is studied analytically using Lie derivatives and numerically with the observability index and condition number obtained from employing an Extended Kalman Filter (EKF). The results highlight the improving benefits of using higher order nonlinear models.

To explain the behavior of HCW dynamics in an EKF with range-only measurements, a classification of ambiguous spacecraft relative orbits in sequential orbit estimation is formulated based on continuous range-only measurements. Using relative orbit elements the ambiguous orbits are categorized into two cases: mirror ambiguous orbits, which conserve the size and shape but transform the orientation of the true relative orbit, and deformed ambiguous orbits, which both distort the shape and change the orientation. Furthermore, it is shown that the inclusion of higher order nonlinearities in the filter model can help resist the tendency of an EKF to converge to the ambiguous orbits.

2.0 INTRODUCTION

Relative orbit estimation is desirable for many types of spacecraft missions, such as formation control and rendezvous. Performing spacecraft maneuvers based only on on-board measurements reduces the total operating cost, and improves safety against communication interruptions with ground stations. Relative navigation between spacecraft in close-proximity essentially corresponds to space-based orbit determination. In particular, range-based and vision-based navigation and estimation of relative orbit have received attention recently, since they have desirable properties of low cost and minimal maintenance.

Several papers have considered relative orbit navigation and estimation from different perspectives. The core problem is to determine the relative orbit between a chief spacecraft and a deputy spacecraft by certain measurements, assuming that the orbit of the chief is prescribed exactly. Huxel and Bishop [1] discussed the effects of using both inertial range measurements from tracking stations and relative range measurements among formation members in the context of two-body dynamics in the inertial frame. Also using two-body inertial dynamics, Yim, *et al.* [2] numerically studied the observability of relative orbit estimation by taking line-of-sight (LOS) measurements with incorporation of J2 perturbation and showed that proper choices of orbital element differences can improve estimation performance. Taking LOS measurement only, Woffiden and Geller [3,4] discussed relative orbit estimation based on the Hill-Clohessey-Wiltshire dynamic model [5,6] and concluded this scenario is unobservable. Using the Lie derivative method, Kaufman, *et al.* [7] showed that with LOS measurement only, the nonlinear relative orbital dynamics are observable under certain geometric conditions. Psiaki [8] considered relative orbit estimation from the view of orbital element differences and widely discussed the improvement of observability by adding J2 perturbation or altering orbital element differences. Rundberg and Lovell [9] discussed the initial relative orbit determination using minimal number of range-only measurements.

In this report, the effects of including nonlinearities in the filter dynamic model on observability in relative orbit estimation for unperturbed circular chief orbits are explored. Four different dynamic models, i.e., first order (HCW), second order, third order and full nonlinear models are employed in an extended Kalman filter along with two different types of measurements: range-only and angles-only. The analytical method of Lie derivatives and the numerical methods of observability index and condition number are applied to analyze the observability in relative orbit estimation with the four different models listed above.

To explain the appearance of ambiguous trajectories using continuous range-only measurements in an EKF, an analytical analysis of ambiguous conditions is presented using relative orbital elements. Subsequently, the enumeration and classification of these trajectories is provided both by using Cartesian coordinates and geometric properties of the relative orbit. The condition of existence for the deformed ambiguous orbit is also shown through the solution of a fourth order polynomial. Finally, as means to exclude ambiguities, we explore the possibility of using higher order nonlinear models to guarantee the uniqueness of the estimated orbit.

3.0 METHODS, ASSUMPTIONS, AND PROCEDURES

Consider two satellites orbiting the Earth where each satellite is modeled as a point mass. Suppose that a *chief* spacecraft is on a circular orbit with a pre-determined orbital radius $r_c \in \mathbb{R}$. In fact, there exist several ways to model spacecraft relative motion, for example describing the motion of each spacecraft individually in the inertial frame, or using a dynamic model of orbital element differences. However, to better visualize the relative motion from the view of the chief spacecraft, the relative motion is described in the chief Local Vertical Local Horizontal (LVLH) frame in this paper.

A LVLH frame is defined as follows. Its origin is located at the chief satellite. The x -axis is along the radial direction from the Earth to the chief, and the y -axis is along the velocity vector of the chief. The z -axis is normal to the orbital plane, and it is parallel to the angular momentum vector of the chief. The angular velocity of the LVLH frame with respect to an inertial frame, expressed in LVLH coordinates, is given by $\boldsymbol{\omega} = [0, 0, n]^T \in \mathbb{R}^3$, where $n = \sqrt{\mu/r_c^3}$ is the mean motion of the chief satellite, and μ denotes the gravitational parameter of the Earth. Note the inertial velocity of the chief expressed in the LVLH frame is given by $\mathbf{v}_c = [0, nr_c, 0]^T \in \mathbb{R}^3$. Let the relative position of a *deputy* spacecraft with respect to the chief spacecraft be given by $\boldsymbol{\rho} = [x, y, z]^T \in \mathbb{R}^3$ in the LVLH frame.

3.1 Dynamics of Relative Motion with Different Nonlinearities

In order to describe the dynamics of relative motion concisely, the state space form $\dot{\mathbf{X}} = \mathbf{F}(\mathbf{X})$ is used, where $\mathbf{X} = [\boldsymbol{\rho}^T \ \dot{\boldsymbol{\rho}}^T]^T = [x, y, z, \dot{x}, \dot{y}, \dot{z}]^T \in \mathbb{R}^6$ are the position and velocity states of the deputy relative to the chief in chief's LVLH frame, and $\mathbf{F}(\mathbf{X})$ is the corresponding vector field. The derivation for dynamic models of different nonlinear orders are based on truncating a Taylor series expansion of two-body relative orbit dynamics at different orders.

First order dynamic model. The first order dynamic model (HCW model) only includes the linear terms from the Taylor expansion in the relative orbit dynamics, and its vector field is given by

$$\mathbf{F}_1(\mathbf{X}) = \begin{bmatrix} \dot{\boldsymbol{\rho}} \\ \ddot{\boldsymbol{\rho}} \end{bmatrix} = \begin{bmatrix} \dot{\boldsymbol{\rho}} \\ -2\boldsymbol{\omega} \times \dot{\boldsymbol{\rho}} + \mathbf{K}\boldsymbol{\rho} \end{bmatrix} \quad (1)$$

where $\mathbf{K} = \text{diag} [3n^2, 0, -n^2]$ is a diagonal matrix.

Second order dynamic model. The second order dynamic model [10] adds second order terms from the Taylor expansion to the first order model, and its vector field is given by

$$\mathbf{F}_2(\mathbf{X}) = \begin{bmatrix} \dot{\boldsymbol{\rho}} \\ \ddot{\boldsymbol{\rho}} \end{bmatrix} = \begin{bmatrix} \dot{\boldsymbol{\rho}} \\ -2\boldsymbol{\omega} \times \dot{\boldsymbol{\rho}} + \mathbf{K}\boldsymbol{\rho} + \boldsymbol{\Gamma}_2 \end{bmatrix} \quad (2)$$

where $\boldsymbol{\Gamma}_2$ represents 2nd order terms, namely

$$\boldsymbol{\Gamma}_2 = \frac{\mu}{r_c^4} \begin{bmatrix} -3x^2 + \frac{3}{2}y^2 + \frac{3}{2}z^2 \\ 3xy \\ 3xz \end{bmatrix} \quad (3)$$

Third order dynamic model. The third order dynamic model [11] adds third order terms from the Taylor expansion to the second order dynamic model, and its vector field is given by

$$\mathbf{F}_3(\mathbf{X}) = \begin{bmatrix} \dot{\boldsymbol{\rho}} \\ \ddot{\boldsymbol{\rho}} \end{bmatrix} = \begin{bmatrix} -2\boldsymbol{\omega} \times \dot{\boldsymbol{\rho}} + \mathbf{K}\dot{\boldsymbol{\rho}} + \boldsymbol{\Gamma}_2 + \boldsymbol{\Gamma}_3 \end{bmatrix} \quad (4)$$

where $\boldsymbol{\Gamma}_3$ represents third order terms

$$\boldsymbol{\Gamma}_3 = \frac{\mu}{r_c^5} \begin{bmatrix} 4x^3 - 6x(y^2 + z^2) \\ -6x^2y + \frac{3}{2}y^3 + \frac{3}{2}yz^2 \\ -6x^2z + \frac{3}{2}z^3 + \frac{3}{2}zy^2 \end{bmatrix} \quad (5)$$

Full nonlinear dynamic model. The full nonlinear dynamic model is the most accurate model considered in this paper. The vector field can be expressed as

$$\mathbf{F}_f(\mathbf{X}) = \begin{bmatrix} \dot{\boldsymbol{\rho}} \\ \ddot{\boldsymbol{\rho}} \end{bmatrix} = \begin{bmatrix} -2\boldsymbol{\omega} \times \dot{\boldsymbol{\rho}} - \boldsymbol{\omega} \times (\boldsymbol{\omega} \times \mathbf{r}_d) - \frac{\mu\mathbf{r}_d}{\|\mathbf{r}_d\|^3} \end{bmatrix} \quad (6)$$

where $\mathbf{r}_d = [r_c + x, y, z]^T \in \mathbb{R}^3$ is the position vector of the deputy relative to the center of the Earth in the chief's LVLH frame.

3.2 Measurements

For the output equation, we assume the chief spacecraft takes relative measurements towards the deputy of either range-only measurements or angles-only measurements.

Range measurements. Range measurements are represented by the magnitude of the relative position vector, i.e.,

$$\mathbf{Y} = \rho = \sqrt{x^2 + y^2 + z^2} \quad (7)$$

Angle measurements. One option to define angle measurements is by using two bearing angles λ and ϕ (shown in Figure 1), namely the measurement

$$\mathbf{Y} = \begin{bmatrix} \lambda \\ \phi \end{bmatrix} \quad (8)$$

where

$$\begin{aligned} \phi &= \text{asin} \frac{z}{\sqrt{x^2 + y^2 + z^2}}, \quad \phi \in \left[-\frac{\pi}{2}, \frac{\pi}{2}\right] \\ \lambda &= \text{atan2}(y, x), \quad \text{if } \text{atan2}(y, x) \in [0, \pi] \\ \lambda &= 2\pi + \text{atan2}(y, x), \quad \text{if } \text{atan2}(y, x) \in (-\pi, 0) \end{aligned} \quad (9)$$

Approved for public release; distribution is unlimited.

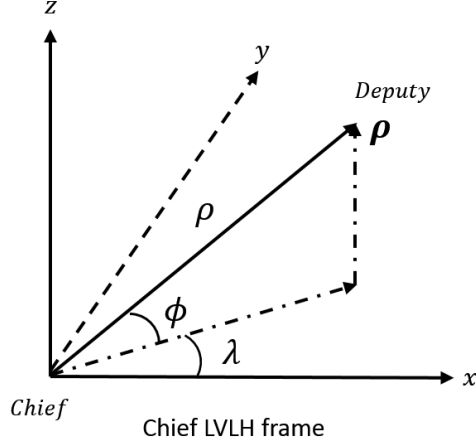


Figure 1. Measurement Relationship in Chief's LVLH Frame

Another option is the equivalent LOS measurement, which is the unit-vector in the relative position direction, i.e.,

$$\mathbf{Y} = \hat{\boldsymbol{\rho}} = \frac{\boldsymbol{\rho}}{\|\boldsymbol{\rho}\|} \quad (10)$$

It is clear to see that the LOS vector $\hat{\boldsymbol{\rho}}$ and two bearing angles (λ, ϕ) are equivalent.

3.3 Analytical Observability Criteria for Nonlinear Systems

Generally, for a nonlinear system given by

$$\begin{aligned} \dot{x} &= f(x) \\ y &= h(x) \\ x(0) &= x_0 \end{aligned} \quad (11)$$

where $x \in \mathbb{R}^n$ and $y \in \mathbb{R}^p$, the system is observable over the interval $[0, T]$ if the mapping from initial state x_0 to output profile $y(0 : T)$ is one to one. It is locally observable over the interval $[0, T]$ if this mapping is locally one to one. A widely accepted tool for checking local observability is the observability rank condition given by Lie derivatives [12, 13]. Let the first order Lie derivative of output $h(x)$ along vector field $f(x)$ be

$$L_f h(x) = \frac{\partial h(x)}{\partial x} f(x) \in \mathbb{R}^{p \times 1} \quad (12)$$

with the n th order Lie derivative defined recursively as

$$L_f^n h(x) = \frac{\partial L_f^{n-1} h(x)}{\partial x} f(x) \in \mathbb{R}^{p \times 1} \quad (13)$$

with zero order Lie-derivative $L_f^0 h = h$. Define an observability matrix $N \in \mathbb{R}^{pn \times n}$ as

$$N(x) = \frac{\partial}{\partial x} \begin{bmatrix} L_f^0 h(x) \\ L_f^1 h(x) \\ \vdots \\ L_f^{n-1} h(x) \end{bmatrix} \quad (14)$$

It has been shown that the system is locally observable at x if the rank of the observability matrix satisfies $\text{rank } N(x) = n$. When applied to linear dynamics, this yields the well-known observability rank condition for linear systems. Note that when there is more than a single measurement type, i.e., $p > 1$, it is possible to satisfy the observability rank condition without need for computing the higher-order Lie derivatives up to the $(n - 1)$ th order. Moreover, it is usually difficult to check higher order rows in $N(x)$, and the practical choice is to stop when $N(x_0)$ has more rows than columns, or at least when $N(x)$ is a square matrix. For this reason, the Lie derivative method can only guarantee observability if the first n rows in matrix $N(x)$ are non-singular, but the method cannot guarantee the unobservability of the nonlinear system.

3.4 Numerical Observability Measure of Nonlinear Systems

The observability rank condition essentially determines whether the system is locally observable over a short period of time in the vicinity of the time at which the observability rank is computed, but it does not tell us how easy it is to observe the system. To overcome this problem, the observability Gramian and some related quantities are introduced.

The observability Gramian measures the sensitivity of the output with respect to the initial condition. For a continuous nonlinear system as in Eq. (11), the observability Gramian is defined as [14]:

$$W_c(x_0, t_0, t_f) = \int_{t_0}^{t_f} \left(\frac{\partial y(\tau)}{\partial x_0} \right)^T \frac{\partial y(\tau)}{\partial x_0} d\tau \quad (15)$$

Corresponding to this definition, the observability Gramian for discrete time systems is defined as:

$$W_d(X_0, t_i, t_f) = \sum_{i=0}^N \Phi^T(i, 0) H_i^T H_i \Phi(i, 0) \quad (16)$$

where N is the number of measurement times, $\Phi(i, 0)$ is the state transition matrix from time $t = t_0$ to time $t = t_i$ satisfying $\dot{\Phi}(t) = \frac{\partial f(x)}{\partial x} \Phi(t)$, and $H = \frac{\partial y}{\partial x}$ is the Jacobian matrix for measurement relationship. It turns out that the observability of a system is deeply related to the eigenvalues and singular values of the observability Gramian, with which a wide variety of different measures have been proposed. Two of most commonly used measures are introduced here.

Waldraff, *et al.* [15] outlined the observability index (OI), which is defined as the smallest singular value of the observability Gramian W_d , i.e.,

$$OI = \min \sigma(W_d) \quad (17)$$

where σ denotes singular value of a matrix. They also discussed that if OI is small, then observation noises can have a large impact on the estimation error. In other words, a larger OI indicates better observability.

Dochain, *et al.* [16] made use of the estimation condition number (CN) for the observability analysis, which is defined as the ratio of largest singular value to the smallest singular value of the observability Gramian W_d , i.e.,

$$CN = \frac{\max \sigma(W_d)}{\min \sigma(W_d)} \quad (18)$$

If CN is large then the effect on the output caused by a small change in the initial condition in one direction can swamp the effect on the output of a change in another direction. In other words the estimation problem is ill-conditioned near states with large local estimation condition number.

4.0 OBSERVABILITY ANALYSIS FOR RELATIVE MOTION WITH LOS MEASUREMENTS

As discussed in the Introduction, Reference [7] applied the Lie derivative method on the full nonlinear dynamic model, resulting in observability conditions for LOS measurements. This paper extends this work to three other dynamic models and discusses observability conditions for each one of them. The general logic is shown as follows:

Consider a general form of vector field \mathbf{F}

$$\mathbf{F}(\mathbf{X}) = \begin{bmatrix} \dot{\boldsymbol{\rho}} \\ \ddot{\boldsymbol{\rho}} \end{bmatrix} = \begin{bmatrix} \dot{\boldsymbol{\rho}} \\ -2\boldsymbol{\omega} \times \dot{\boldsymbol{\rho}} + \dots \end{bmatrix} \quad (19)$$

For the relative motion models with different orders of nonlinearities, \mathbf{F} can be replaced by \mathbf{F}_1 , \mathbf{F}_2 , \mathbf{F}_3 or \mathbf{F}_f , and the LOS measurement \mathbf{Y} can be expressed as

$$\mathbf{Y} = \hat{\boldsymbol{\rho}} = \frac{\boldsymbol{\rho}}{\|\boldsymbol{\rho}\|} \quad (20)$$

With certain order of vector field \mathbf{F} and LOS measurement \mathbf{Y} , we can derive the first three rows of N by

$$N_3 = \begin{bmatrix} \frac{\partial \hat{\rho}}{\partial \boldsymbol{\rho}} & \frac{\partial \hat{\rho}}{\partial \dot{\boldsymbol{\rho}}} \\ \frac{\partial \dot{\hat{\rho}}}{\partial \boldsymbol{\rho}} & \frac{\partial \dot{\hat{\rho}}}{\partial \dot{\boldsymbol{\rho}}} \\ \frac{\partial \ddot{\hat{\rho}}}{\partial \boldsymbol{\rho}} & \frac{\partial \ddot{\hat{\rho}}}{\partial \dot{\boldsymbol{\rho}}} \end{bmatrix} \quad (21)$$

The key to observability analysis is to find the conditions that guarantee the full rank of the N_3 matrix. However, the process of deriving the full rank condition for N_3 is complicated and therefore not shown here. Readers may refer to Reference [7] to have a better understanding. Instead, we extend the observability conditions to relative motion models with different orders of nonlinearities.

Observability conditions for first order model. The observability problem with linear dynamics based on LOS measurements has been widely discussed. Most notably, Woffiden and Geller [3] have proved that based on linear dynamics of the HCW model, the system is unobservable by taking angles-only measurements. In this paper, by substituting vector field \mathbf{F}_1 into Eq. (21), we find that the N_3 matrix loses full rank for linear dynamics, meaning that the Lie derivative analysis also implies the unobservability of linear dynamics with angles-only measurements.

Observability conditions for second order model. Substituting vector field \mathbf{F}_2 in Eq. (3) into Eq. (21), the resulting observable conditions are obtained as:

$$\begin{aligned} (i) \quad & \text{when } \boldsymbol{\rho} \times \dot{\boldsymbol{\rho}} = \mathbf{0}, \Gamma_2 \nparallel \hat{\boldsymbol{\rho}} \text{ and } \boldsymbol{\rho}^T(\Gamma_2 \times (\boldsymbol{\omega} \times \boldsymbol{\rho})) \neq 0 \\ (ii) \quad & \text{when } \boldsymbol{\rho} \times \dot{\boldsymbol{\rho}} \neq \mathbf{0}, \Gamma_2 \nparallel \hat{\boldsymbol{\rho}} \text{ and } \boldsymbol{\rho}^T(\Gamma_2 \times \mathbf{v}_{rel}) \neq 0 \end{aligned} \quad (22)$$

where $\mathbf{v}_{rel} = \dot{\boldsymbol{\rho}} + \boldsymbol{\omega} \times \boldsymbol{\rho}$ is the velocity vector of deputy relative to chief.

Observability conditions for third order model. Substituting vector field \mathbf{F}_3 in Eq. (4) into Eq. (21), the resulting observable conditions are obtained as:

$$\begin{aligned} (i) \quad & \text{when } \boldsymbol{\rho} \times \dot{\boldsymbol{\rho}} = \mathbf{0}, (\boldsymbol{\Gamma}_2 + 2\boldsymbol{\Gamma}_3) \nparallel \hat{\boldsymbol{\rho}} \text{ and } \boldsymbol{\rho}^T((\boldsymbol{\Gamma}_2 + 2\boldsymbol{\Gamma}_3) \times (\boldsymbol{\omega} \times \boldsymbol{\rho})) \neq 0 \\ (ii) \quad & \text{when } \boldsymbol{\rho} \times \dot{\boldsymbol{\rho}} \neq \mathbf{0}, (\boldsymbol{\Gamma}_2 + 2\boldsymbol{\Gamma}_3) \nparallel \hat{\boldsymbol{\rho}} \text{ and } \boldsymbol{\rho}^T((\boldsymbol{\Gamma}_2 + 2\boldsymbol{\Gamma}_3) \times \mathbf{v}_{rel}) \neq 0 \end{aligned} \quad (23)$$

Observability conditions for full nonlinear model. Substituting vector field \mathbf{F}_f in Eq. (6) into Eq. (21), the resulting observable conditions are obtained as:

$$\begin{aligned} (i) \quad & \text{when } \boldsymbol{\rho} \times \dot{\boldsymbol{\rho}} = \mathbf{0}, \mathbf{a}_f \nparallel \hat{\boldsymbol{\rho}} \text{ and } \boldsymbol{\rho}^T(\mathbf{a}_f \times (\boldsymbol{\omega} \times \boldsymbol{\rho})) \neq 0 \\ (ii) \quad & \text{when } \boldsymbol{\rho} \times \dot{\boldsymbol{\rho}} \neq \mathbf{0}, \mathbf{a}_f \nparallel \hat{\boldsymbol{\rho}} \text{ and } \boldsymbol{\rho}^T(\mathbf{a}_f \times \mathbf{v}_{rel}) \neq 0 \end{aligned} \quad (24)$$

where \mathbf{a}_f can be expressed as

$$\mathbf{a}_f = \boldsymbol{\omega} \times (\boldsymbol{\omega} \times \mathbf{r}_c) + \frac{\mu \mathbf{r}_c}{r_d^3} + \frac{3\mu \mathbf{r}_d \mathbf{r}_d^T}{r_d^5} \boldsymbol{\rho} \quad (25)$$

It is noted that even if Eq. (22), (23) or (24) is violated, it only implies that the corresponding order of dynamic model is unobservable at that specific time epoch and does not mean the whole measurement profile can not result in an observable system. In other words, when the observable conditions are violated at a certain time epoch, the LOS measurements make little or no contribution on improving the observability. On the contrary, for linear dynamics, Woffiden and Geller [3] have drawn a decisive conclusion that the system is unobservable with LOS measurements regardless of the number of measurements being taken.

5.0 NUMERICAL RESULTS FOR OBSERVABILITY ANALYSIS OF RELATIVE MOTION

We choose one primary scenario of relative motion between chief and deputy orbits shown in Table 1. Note that the orbital elements difference are chosen such that the scales of relative motion on three directions of chief's LVLH frame are comparable as shown in Figure 2.

Table 1. Orbital Element Differences for Primary Simulation Case

	a (km)	e	i	Ω	ω	M_0
Chief	7100	0	0°	0°	0°	0°
Deputy	7100	0.005	0.3°	0°	0°	0.1°

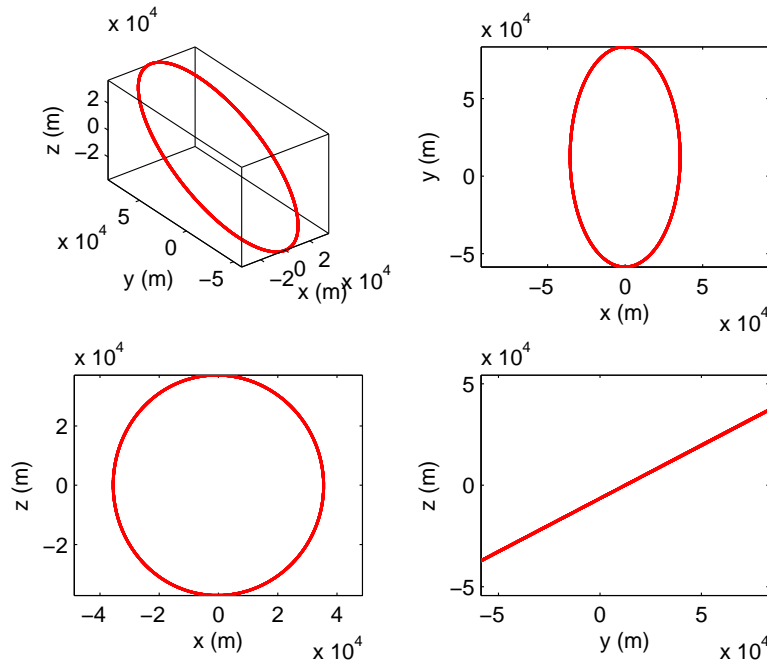


Figure 2. The True Relative Orbit in Chief's LVLH Frame with 3-D Projections

Furthermore, we evaluate the observability measure for different order of nonlinearities based on local observability Gramian and process range-only and angles-only measurements with the EKF, using the full nonlinear model as the truth model.

For both range-only and angles-only measurements, the initial state deviation for EKF is

$$\delta \mathbf{X}_0 = [1000, -1000, 1000, 1, 1, -1](\text{m}, \text{m/s}) \quad (26)$$

and the initial covariance of the state is chosen as

$$P_0 = \text{diag} [1.8 \times 10^7, 1.8 \times 10^7, 1.8 \times 10^7, 18, 18, 18](\text{m}^2, \text{m}^2/\text{s}^2) \quad (27)$$

The sample time is $\Delta t = 10$ seconds. For range-only measurements, the measurement covariance matrix is assumed to be $R = 20^2 \text{ m}^2$. For angles-only measurements, $R = \text{diag} [2.7416 \times 10^{-7}, 2.7416 \times 10^{-7}] \text{ rad}^2$, which corresponds to the variances of two bearing angles $\sigma_\lambda = \sigma_\phi = 0.03^\circ$. Since different orders of nonlinearities will be considered, different levels of process noise will be applied to different dynamical models separately.

5.1 Results for Four Models with Different Nonlinearities

Figure 3 illustrates the simulation results for the EKF based on the four different relative motion models with range-only measurements, in which the red line denotes the true relative orbit and the blue line denotes the estimated orbit. From Figure 3(a), it is clear that the Kalman filter based on the HCW model cannot estimate the true states effectively and manifests the inability to distinguish between two orbits with the same range information. In Figure 3(b), using the second order dynamic model, the filter successfully captures the motion of true relative orbit, even though its accuracy may not be satisfactory at the beginning. In Figure 3(c), with a dynamic model truncated at third order, the estimated relative orbit very closely follows the true relative orbit. In fact, it is surprising that the estimated results in (c) are almost as good as the results in (d). This indicates that a third order model is required to accurately characterize the relative motion for this particular case. It is expected that for cases where the chief and deputy are closer together, the results utilizing a second order model may be more similar to those obtained with a third order or full nonlinear model.

Table 2 summarizes the performance of the EKF with different nonlinearities for range-only measurements. OI and CN are the observability index and condition number of the observability Gramian. e_ρ indicates the estimation position error root mean square (RMS) and is defined as

$$e_\rho = \sqrt{\frac{1}{N} \sum_{k=0}^N \|(\hat{\rho}_k - \rho_k)\|^2} \quad (28)$$

where $\hat{\rho}_k = [\hat{x}_k, \hat{y}_k, \hat{z}_k]^T$ is the k th estimated relative position vector and ρ_k is the k th true relative position vector. $e_{\dot{\rho}}$ denotes the estimation velocity error, i.e.,

$$e_{\dot{\rho}} = \sqrt{\frac{1}{N} \sum_{k=0}^N \|(\hat{\dot{\rho}}_k - \dot{\rho}_k)\|^2} \quad (29)$$

where $\hat{\dot{\rho}}_k = [\hat{\dot{x}}_k, \hat{\dot{y}}_k, \hat{\dot{z}}_k]^T$.

Table 2. Performance of EKF Based on Range-only Measurements

	OI	CN	e_ρ (m)	$e_{\dot{\rho}}$ (m/s)	$\lambda_{max}(P)$	$\det(P)$
1 st	1.89×10^{-15}	2.93×10^{16}	5.15×10^4	54.20	2.36×10^3	6.00×10^{-4}
2 nd	1.61×10^{-12}	1.38×10^{13}	1.11×10^2	0.62	4.73×10^2	6.16×10^{-9}
3 rd	1.33×10^{-9}	3.78×10^{10}	23.26	0.064	8.63	2.41×10^{-19}
full	1.63×10^{-9}	3.43×10^{10}	21.83	0.052	7.62	5.23×10^{-20}

In Table 2, $\lambda_{max}(P)$ is the maximum eigenvalue of covariance matrix P . It indicates the variance of worst estimated state among all the six states. $\det(P)$ is the determinant of matrix P , which can be interpreted as the overall performance of EKF since $\det(P) = \lambda_1 \lambda_2 \dots \lambda_6$ is the product of the variances of the six states.

From the first two columns of Table 2, OI increases and CN decreases drastically from first order to second order and second order to third order dynamic models. However, changing from third order model to full nonlinear model, OI and CN only differ slightly. It is noted that all the other parameters, e_ρ , $e_{\dot{\rho}}$, $\lambda_{max}(P)$ and $\det(P)$ all follow the same pattern as with OI and CN . This observation agrees with the simulation results in Figure 3.

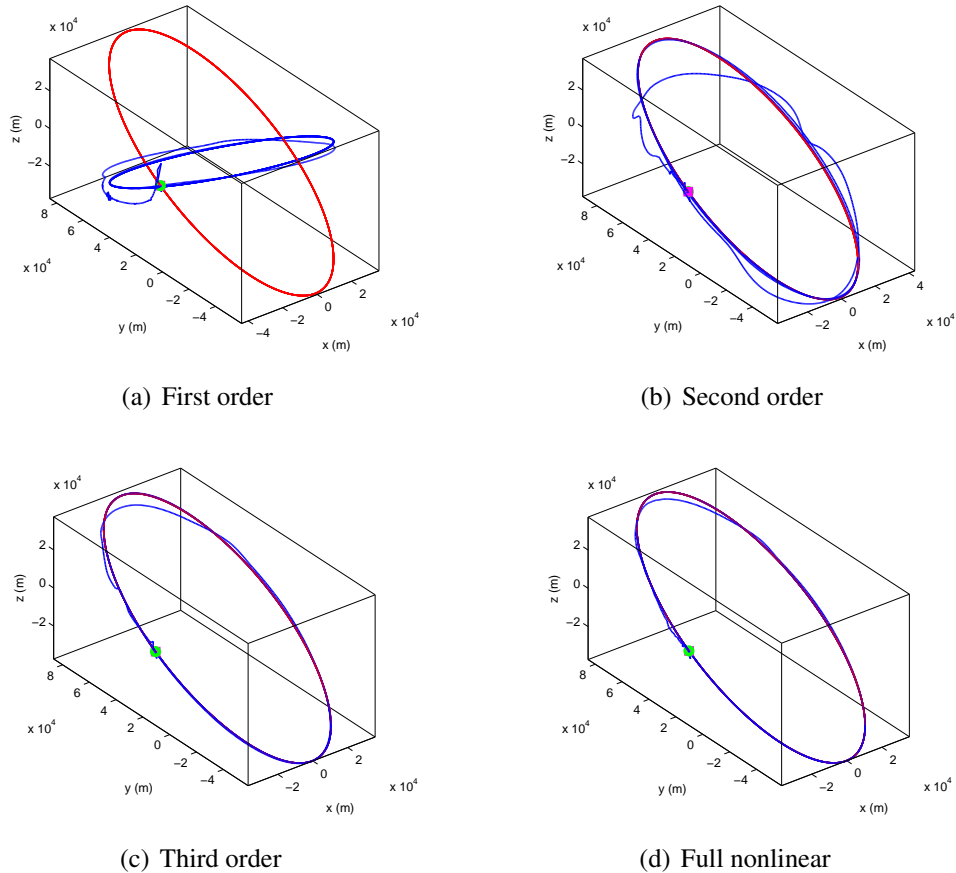


Figure 3. True and Estimated Orbits with Range-only Measurements

With angles-only measurements, the simulation results are illustrated in Figure 4 and Table 3. Again, the observability changes greatly from the first order to second order and from second order to third order dynamic models, while the estimation results of third order and full nonlinear order models are almost indistinguishable.

However, compared with the range-only results for the HCW model shown in Figure 3(a), the estimated orbits with angles-only measurements illustrated in Figure 4(a) are shrunk and keep the shape of the true orbit instead of being disoriented. This is mainly because of the incapability of EKF with angles-only measurement on capturing range information, which has been proposed by Woffiden and Geller [3] as a scalar ambiguity of angles-only measurements based on the linear dynamics.

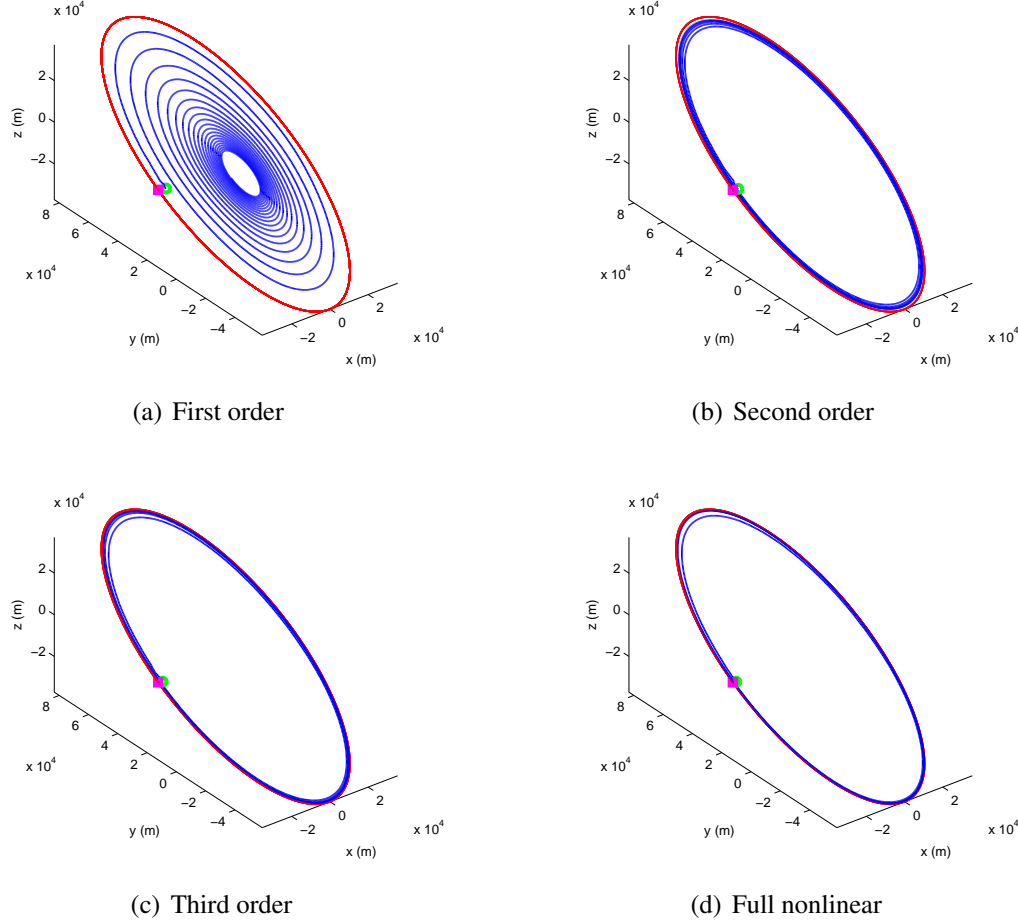


Figure 4. True and Estimated Orbits with Angles-only Measurements

Table 3. Performance of EKF Based on Angles-only Measurements

	OI	CN	e_p (m)	$e_{\dot{p}}$ (m/s)	$\lambda_{max}(P)$	$\det(P)$
1 st	2.27×10^{-16}	5.24×10^{17}	4.27×10^4	44.47	781.43	1.83×10^{-9}
2 nd	1.75×10^{-14}	1.41×10^{14}	1.96×10^2	1.95	136.51	2.48×10^{-13}
3 rd	7.32×10^{-10}	3.85×10^{10}	3.52	0.035	42.735	2.27×10^{-23}
full	7.41×10^{-10}	3.62×10^{10}	2.81	0.029	38.729	3.40×10^{-24}

5.2 Effects of Nonlinearities on the Observability of Different Configurations

In this section, we study how observability changes with different nonlinear filter models through the variation of orbital element differences. The methodology is to vary a certain orbit element difference and compare the improvement of OI and CN between adjacent dynamic models (e.g. first and second order, second and third order, and third order and full nonlinear).

Figure 5 illustrates the change in observability when varying inclination difference. Figures 5(a) and 5(b) are cases for range measurements, while Figures 5(c) and 5(d) are cases for angle measurements. From these plots, we find that with increased inclination difference δi , the observability difference improves almost uniformly (indicated by the increasing $\log OI_j/OI_i$ and $\log CN_i/CN_j, j > i$). This means that higher order nonlinearities grant extra benefits when inclination difference is enlarged. Figure 6 and 7 also illustrate cases for variation of mean anomaly differences and eccentricity differences. From the results, the same conclusion can be drawn as with variation of inclination difference.

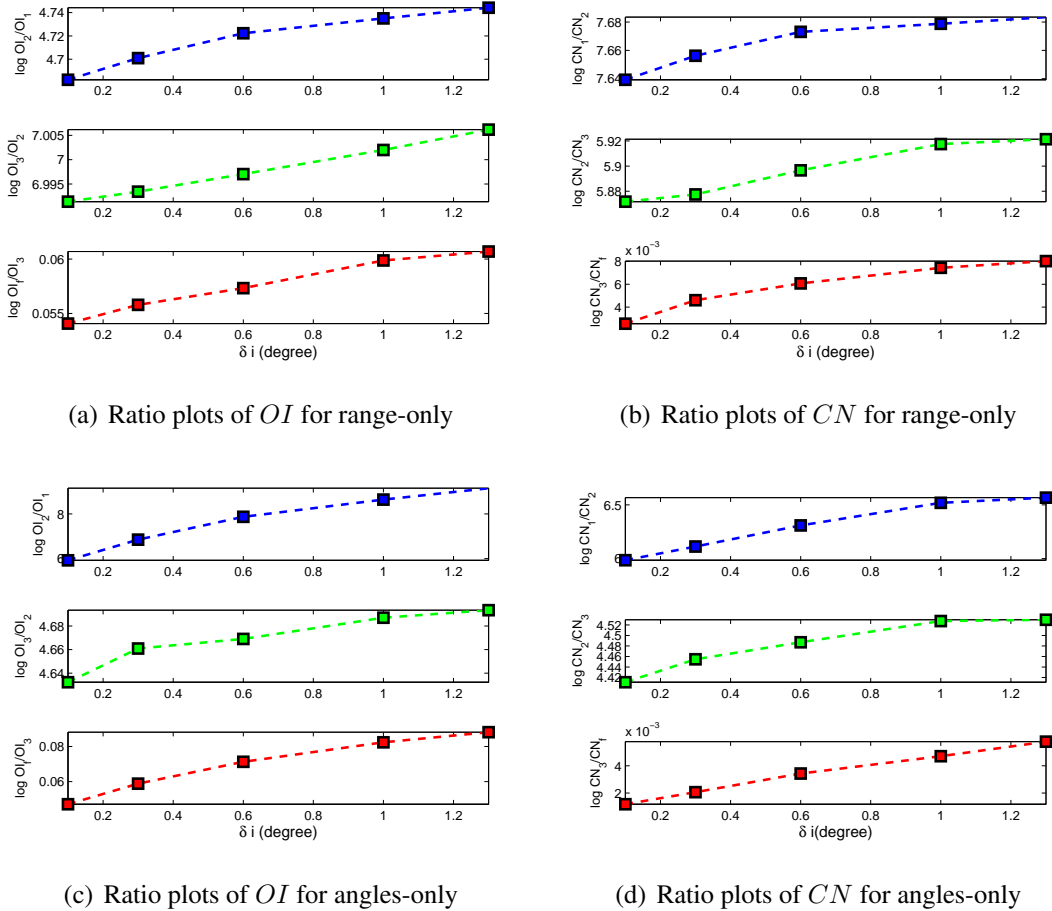
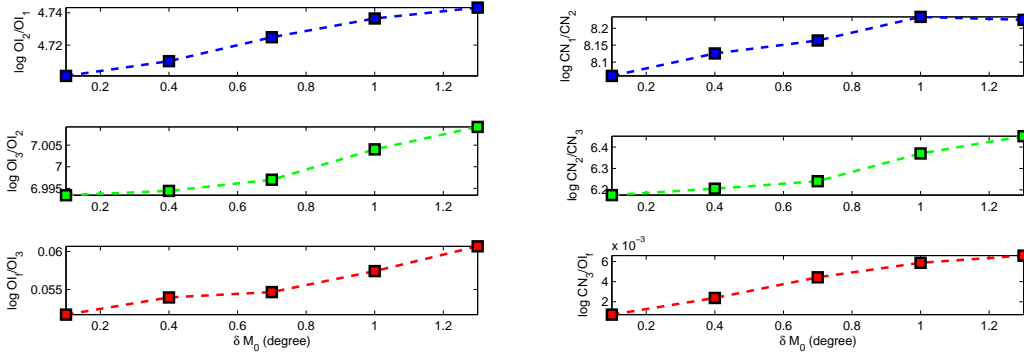
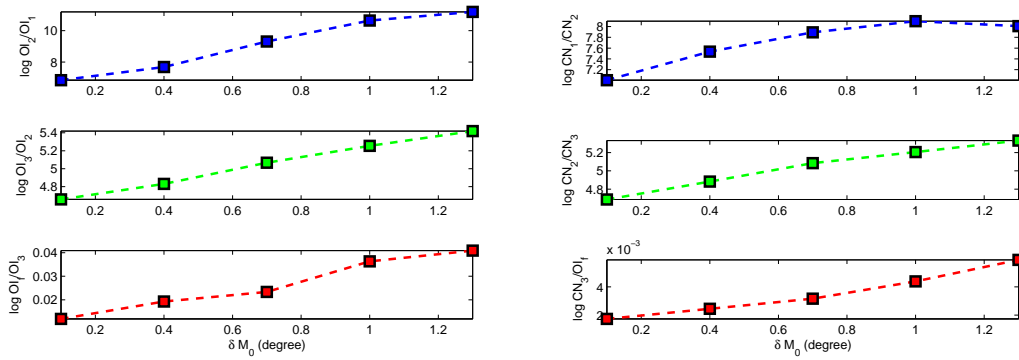


Figure 5. Ratio Plots of OI and CN with Varying Inclination Difference



(a) Ratio plots of OI for range-only measurements (b) Ratio plots of CN for range-only measurements



(c) Ratio plots of OI for angles-only

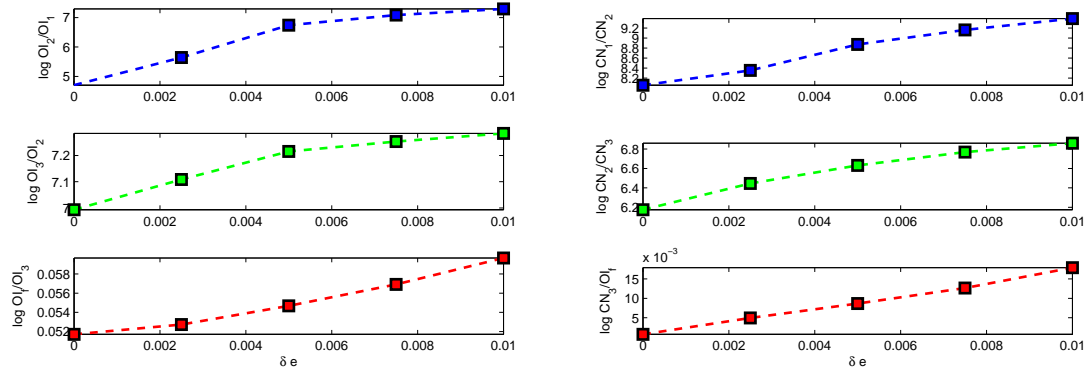
(d) Ratio plots of CN for angles-only measurements

Figure 6. Ratio Plots of OI and CN with Varying Mean Anomaly Difference

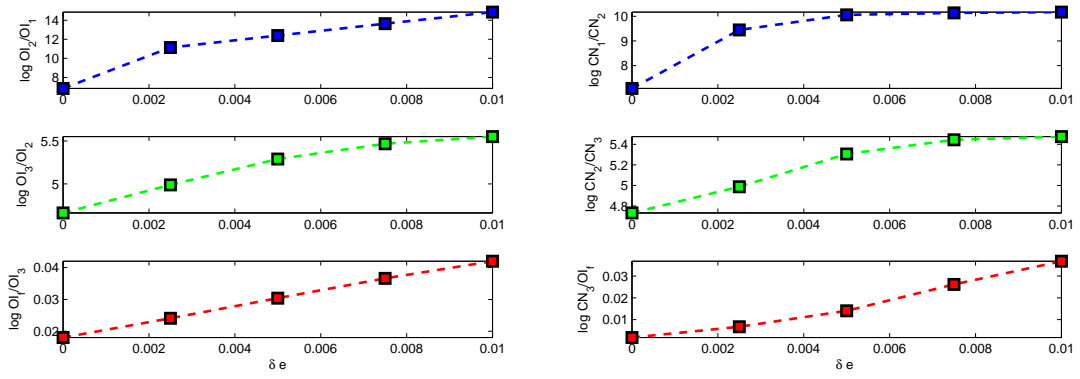
Figures 8 and 9 present the change of OI and CN for variation of inclination difference with range-only and angles-only measurements separately. From these results, the OI and CN of the third order model follow very closely to those of the full nonlinear model for both range-only and angles-only measurements as the inclination difference δi increases. With increasing inclination difference, the advantages of using higher order models become more obvious, particularly for including second and third order terms.

However, the plots of the second order model drift away from the full nonlinear model, meaning that the second order model cannot accurately capture all the properties of relative orbital motion of the true model. With no surprise, the first order dynamic model gives the worst performance among all the relative motion models because of its assumption of close proximity on which the linearization is valid.

We also notice that there exists tuning point in Figures 8 and 9. For example, in Figure 8(a), the maximum value of OI appears between $\delta i = 0.2^\circ$ and $\delta i = 0.8^\circ$, and the corresponding value of δi differs slightly between systems with different nonlinearities.



(a) Ratio plots of OI for range-only measurements (b) Ratio plots of CN for range-only measurements



(c) Ratio plots of OI for angles-only measurements (d) Ratio plots of CN for angles-only measurements

Figure 7. Ratio Plots of OI and CN with Varying Eccentricity Difference

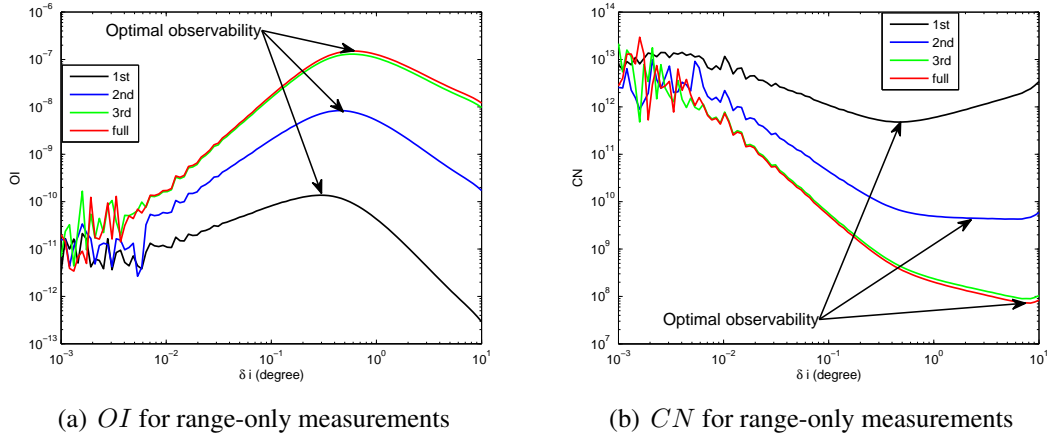


Figure 8. Plots of OI and CN for Different Orders of Nonlinearities (Range-only)

To explain this behavior, recall that OI measures the worst observability among all six states in relative orbit estimation and the filter actually uses the change of range information to decide the deputy's orbit, i.e., the x , y , z coordinates of deputy in chief's LVLH frame. From $\rho = \sqrt{x^2 + y^2 + z^2}$, we have $\delta\rho = \frac{\epsilon}{\rho}\delta\epsilon$, where ϵ denotes x , y or z . Therefore, it is clear that when ϵ is the smallest among all three coordinates, it will be the most insensitive state regarding the change of range, and therefore the least observable state. From Figure 10, we can see that when $\delta i < 0.3^\circ$, the maximum scale in z direction is less than that in x and y direction, making z coordinates least observable. However, when $\delta i > 0.8^\circ$, the scale of z coordinates becomes the dominant, making x coordinates least observable. This observation agrees with the occurrence of the maximum value of OI between $\delta i = 0.2^\circ$ and $\delta i = 0.8^\circ$. Furthermore, the slightly different peak values of δi come from the use of dynamic models with different orders of nonlinearities.

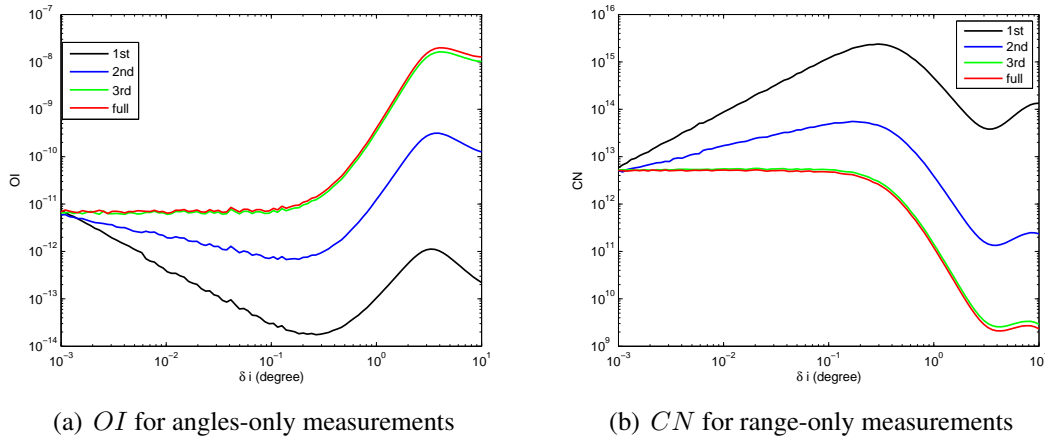


Figure 9. Plots of OI and CN for Different Orders of Nonlinearities (Angles-only)

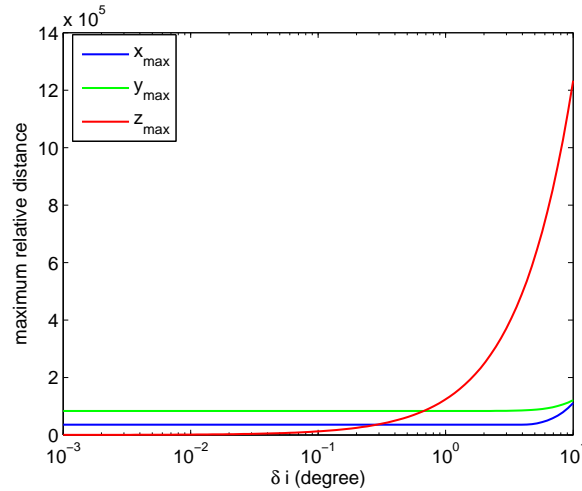


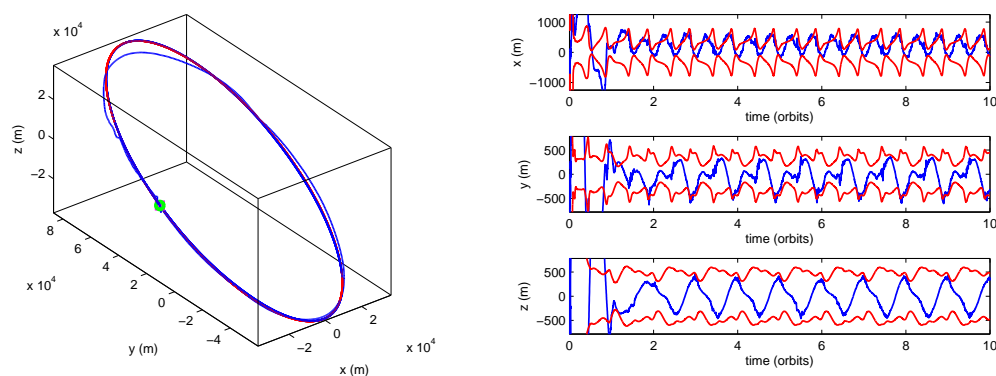
Figure 10. Maximum Relative Distance in Three Directions with Increasing δi

6.0 AMBIGUOUS ORBITS OF HCW MODEL WITH RANGE-ONLY MEASUREMENTS

6.1 Definition of Ambiguous Orbits

In the previous section, we get a glimpse of the weakness of the HCW-based EKF with range-only measurements on relative orbit estimation in Figure 3(a). However, when executing a series of simulations with HCW dynamic model, the estimated orbits converge to several different orbits randomly.

First Case: True relative orbit. The results for the first case are shown in Figure 11. From Figure 11(a), we can see that the estimated orbit follows fairly closely to the true orbit. From Figure 11(b), even though the estimation error is still in the scale of 500 m, the filter successfully keeps the estimated trajectory from diverging.



(a) True vs. estimated orbits (red: true orbit, blue: estimated orbit) (b) Position error (blue: estimation error, red: 3σ covariance envelop)

Figure 11. First Case of Ambiguity Using HCW Based EKF

Second Case: Mirror ambiguous orbit. From Figure 12(a), the estimated orbit (blue line) looks like a mirror image of the true orbit (red line), which indicates the two orbits have same shape and size. Furthermore, in Figure 12 (b), (c) and (d), the in-plane xy motion is described well by the estimated orbit, but the out-of-plane z motion is poorly estimated.

Third Case: Deformed ambiguous orbit. Figure 13 illustrates the trajectory of the true orbit (red line) and the deformed estimated orbit (blue line). Compared with the true orbit, the in-plane xy motion of the estimated orbit is reduced, and the out-of-plane z motion is enlarged. It appears that the EKF with HCW dynamics overestimated the z motion to compensate for the underestimated xy motion to meet the range requirements. Also, the orientation of the estimated orbit is different from the true orbit.

For the following discussion, we will discuss the existence of these ambiguous orbits and their effects on the performance of a filter. For convenience, we make the following definition. An orbit is defined as an ambiguous orbit of the true orbit by range if it shares the

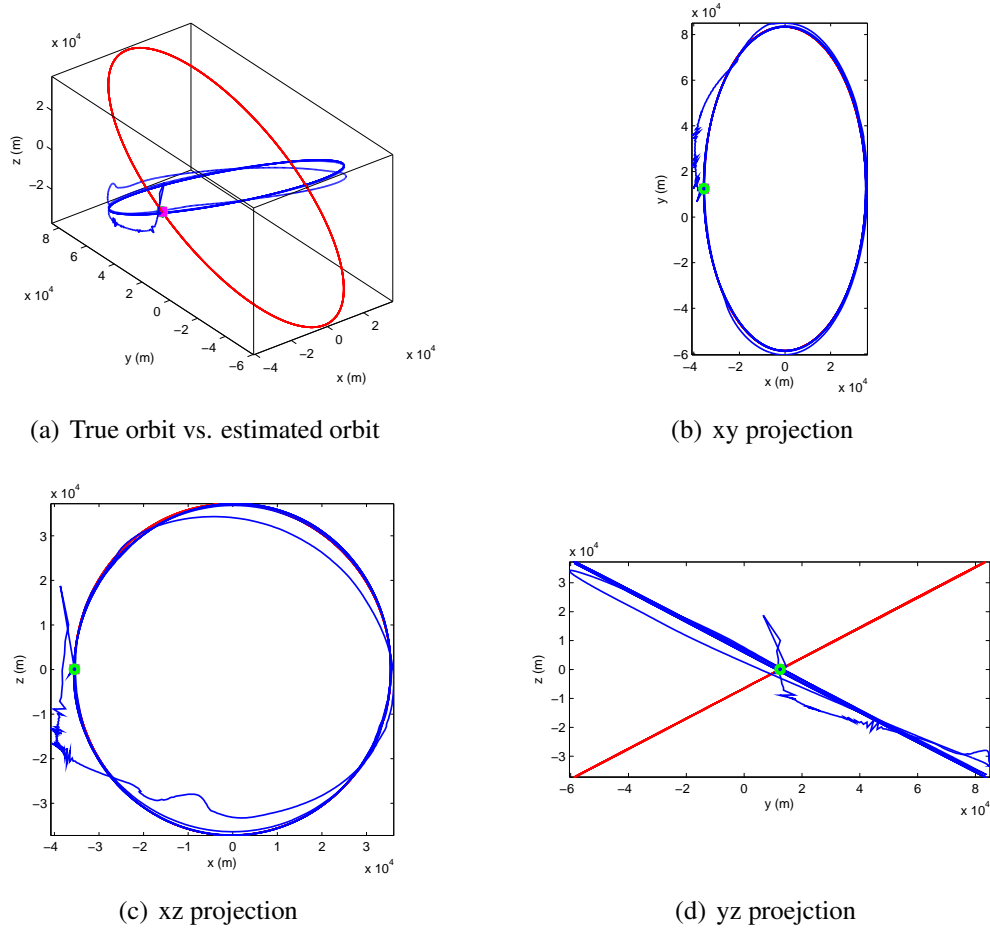


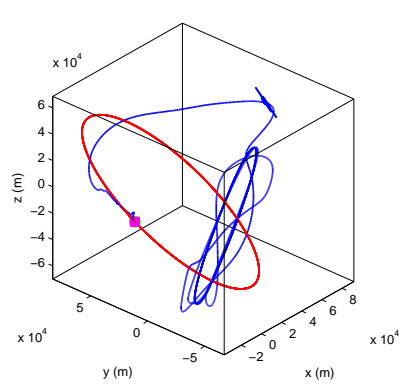
Figure 12. Second Case of Ambiguity Using HCW Based EKF

same range history with the true orbit. Namely, $\rho'(t) = \rho(t)$ for all $t > 0$, where $\rho(t)$ and $\rho'(t)$ are the ranges of the true and ambiguous orbits at time t respectively. Furthermore, if the ambiguous orbit conserves the size and shape of the true orbit then it is classified as a mirror ambiguous orbit; otherwise, it is classified as a deformed ambiguous orbit.

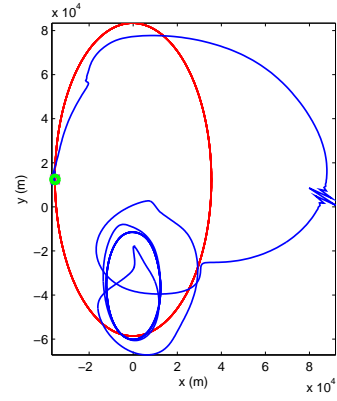
To analyze the ambiguous relative orbits, we utilize the solution of the HCW equation (Eq. (2) expressed in terms of relative orbit elements (ROEs) [17],

$$\begin{aligned} x(t) &= -\frac{a_e}{2} \cos(\beta) + x_d \\ y(t) &= a_e \sin(\beta) + y_d \\ z(t) &= z_m \cos(\psi) \end{aligned} \quad (30)$$

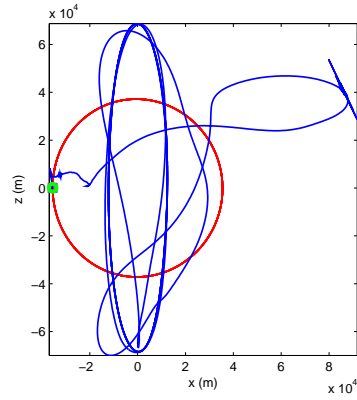
where a_e , x_d , z_m are constant and $y_d(t) = y_{d0} - \frac{3}{2}n x_d t$, $\beta(t) = \beta_0 + nt$ and $\psi(t) = \psi_0 + nt$ are time dependent. It is clear that $(a_e, z_m, x_d, y_{d0}, \beta_0, \psi_0)$ are six constants that can be used



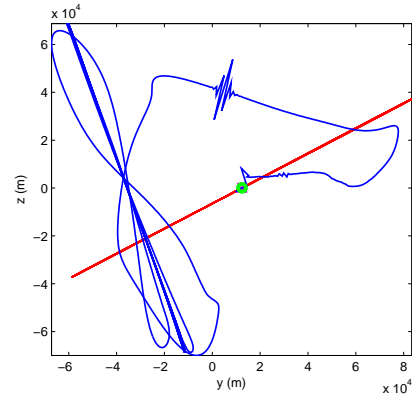
(a) True orbit vs. estimated orbit



(b) xy projection



(c) xz projection



(d) yz proejction

Figure 13. Third Case of Ambiguity Using HCW Based EKF

to represent relative orbits. The square of range ρ at time t can be expressed as

$$\begin{aligned}
 \rho^2(t) &= x^2(t) + y^2(t) + z^2(t) \\
 &= \frac{5}{8}a_e^2 + \frac{1}{2}z_m^2 + y_{d0}^2 \\
 &\quad + \left[-\frac{3}{8}a_e^2 \cos(2\beta_0) + \frac{1}{2}z_m^2 \cos(2\psi_0) \right] \cos(2nt) \\
 &\quad + \left[\frac{3}{8}a_e^2 \sin(2\beta_0) - \frac{1}{2}z_m^2 \sin(2\psi_0) \right] \sin(2nt) \\
 &\quad + 2a_e y_{d0} \sin(\beta_0) \cos(nt) + 2a_e y_{d0} \cos(\beta_0) \sin(nt) \\
 &\quad - 3a_e x_d \sin(\beta_0) nt \cos(nt) - 3a_e x_d \cos(\beta_0) nt \sin(nt) \\
 &\quad - 3x_d y_{d0} nt + \frac{9}{4}x_d^2 t^2
 \end{aligned} \tag{31}$$

Since the nine basis functions in Eq. (31) are linearly independent, the following nine identities must be satisfied for $\rho'^2(t) = \rho^2(t)$.

$$5a_e^2 + 4z_m^2 + 8y_{d0}^2 = 5a_e'^2 + 4z_m'^2 + 8y_{d0}'^2 \quad (32)$$

$$3a_e^2 \cos(2\beta_0) - 4z_m^2 \cos(2\psi_0) = 3a_e'^2 \cos(2\beta_0') - 4z_m'^2 \cos(2\psi_0') \quad (33)$$

$$3a_e^2 \sin(2\beta_0) - 4z_m^2 \sin(2\psi_0) = 3a_e'^2 \sin(2\beta_0') - 4z_m'^2 \sin(2\psi_0') \quad (34)$$

$$a_e y_{d0} \sin(\beta_0) = a_e' y_{d0}' \sin(\beta_0') \quad (35)$$

$$a_e y_{d0} \cos(\beta_0) = a_e' y_{d0}' \cos(\beta_0') \quad (36)$$

$$a_e x_d \sin(\beta_0) = a_e' x_d' \sin(\beta_0') \quad (37)$$

$$a_e x_d \cos(\beta_0) = a_e' x_d' \cos(\beta_0') \quad (38)$$

$$x_d y_{d0} = x_d' y_{d0}' \quad (39)$$

$$x_d^2 = x_d'^2 \quad (40)$$

where the primed quantities correspond to the ambiguous orbit. It is noted that if the non-drifting condition $x_d = 0$ is satisfied, Eqs. (37-40) will vanish. In the following section, we first discuss the ambiguity under the non-drifting condition (Eqs. (32-36)) and then check the validity of the ambiguity once the non-drifting assumption is violated. First, however, we observe that Eqs. (35) and (36) yield

$$|a_e y_{d0}| = |a_e' y_{d0}'| \quad (41)$$

6.2 Mirror Ambiguous Orbits

A mirror ambiguous orbit must have the same magnitude of in-plane and out-of-plane motion as the true orbit, i.e., $|a_e| = |a_e'|$ and $|z_m| = |z_m'|$. Two cases are considered.

Case 1: $a_e y_{d0} = a_e' y_{d0}'$.

This case yields either

$$a_e' = a_e \quad (42)$$

$$y_{d0}' = y_{d0} \quad (43)$$

or,

$$a_e' = -a_e \quad (44)$$

$$y_{d0}' = -y_{d0} \quad (45)$$

Substituting $a_e y_{d0} = a_e' y_{d0}'$ into Eqs. (35) and (36), we obtain

$$\beta_0' = \beta_0 \quad , \quad \text{for } \beta_0 \in [0, 2\pi) \quad (46)$$

Then substituting Eqs. (42-43) or (44-45) into Eq. (32), we obtain $z_m^2 = z_m'^2$ yielding

$$z_m' = z_m \quad (47)$$

$$z_m' = -z_m \quad (48)$$

Finally, with the substitution Eqs. (42-48) into Eq. (33), we have

$$\psi'_0 = \psi_0 \quad (49)$$

$$\psi'_0 = \psi_0 + \pi \quad (50)$$

for $\psi \in [0, 2\pi)$. This yields eight non-unique possible combinations of the initial ROEs.

Case 2: $a_e y_{d0} = -a'_e y'_{d0}$.

As in Case 1, this also yields eight non-unique initial ROE combinations.

These 16 cases contain redundancy in terms of initial Cartesian coordinates, because the initial Cartesian coordinates uniquely determine an orbit, whereas ROEs do not. The transformation from initial ROEs to initial Cartesian states [17] is

$$\begin{aligned} x_0 &= -\frac{a_e}{2} \cos \beta_0 \\ y_0 &= a_e \sin \beta_0 + y_{d0} \\ z_0 &= z_m \cos \psi_0 \\ \dot{x}_0 &= \frac{na_e}{2} \sin \beta_0 \\ \dot{y}_0 &= na_e \cos \beta_0 \\ \dot{z}_0 &= -nz_m \sin \psi_0 \end{aligned} \quad (51)$$

With the transformation in Eq (51), it can be shown that the total number of Cartesian initial states that result in orbits with the same range history is four including the true orbit and three mirror ambiguous orbits. Table 4 lists these orbits as (a), (b), (c) and (t) (which stands for the true orbit). For the case of drifting orbit, it is easy to check that the foregoing 16 ROEs combinations in Case 1 and 2 also satisfy Eqs. (37-40). Therefore, the drifting phenomenon does not exclude these three mirror ambiguous orbits.

Table 4. Types of Mirror Ambiguous Orbits in Initial Cartesian Coordinates

	x'_0	\dot{x}'_0	y'_0	\dot{y}'_0	z'_0	\dot{z}'_0
(t)	x_0	\dot{x}_0	y_0	\dot{y}_0	z_0	\dot{z}_0
(a)	x_0	\dot{x}_0	y_0	\dot{y}_0	$-z_0$	$-\dot{z}_0$
(b)	$-x_0$	$-\dot{x}_0$	$-y_0$	$-\dot{y}_0$	z_0	\dot{z}_0
(c)	$-x_0$	$-\dot{x}_0$	$-y_0$	$-\dot{y}_0$	$-z_0$	$-\dot{z}_0$

To illustrate mirror ambiguous orbits graphically, one periodic true relative orbit under HCW dynamics is chosen with initial condition shown in Table 5. Figure 14(a) illustrates the three mirror ambiguous orbits along with the true relative orbit ((t): red line, (a): blue line, (b): green line, (c): black line). It is easy to see that the four orbits generate the same range history $\rho(t)$ due to the symmetry of the orbits. The y-z projection of the four orbits shown in Figure 14(d) can easily distinguish different ambiguous orbits by the inclination of the relative orbit with respect to the y-axis in the y-z plane (indicated by the slope of the orbit in the y-z projection) and the offset in the y direction, i.e., y_{d0} .

Table 5. Initial Condition for True Relative Orbit

x_0 (km)	y_0 (km)	z_0 (km)	\dot{x}_0 (m/s)	\dot{y}_0 (m/s)	\dot{z}_0 (m/s)
-35.51	12.45	0.065	0.66	$-2nx_0$	39.43

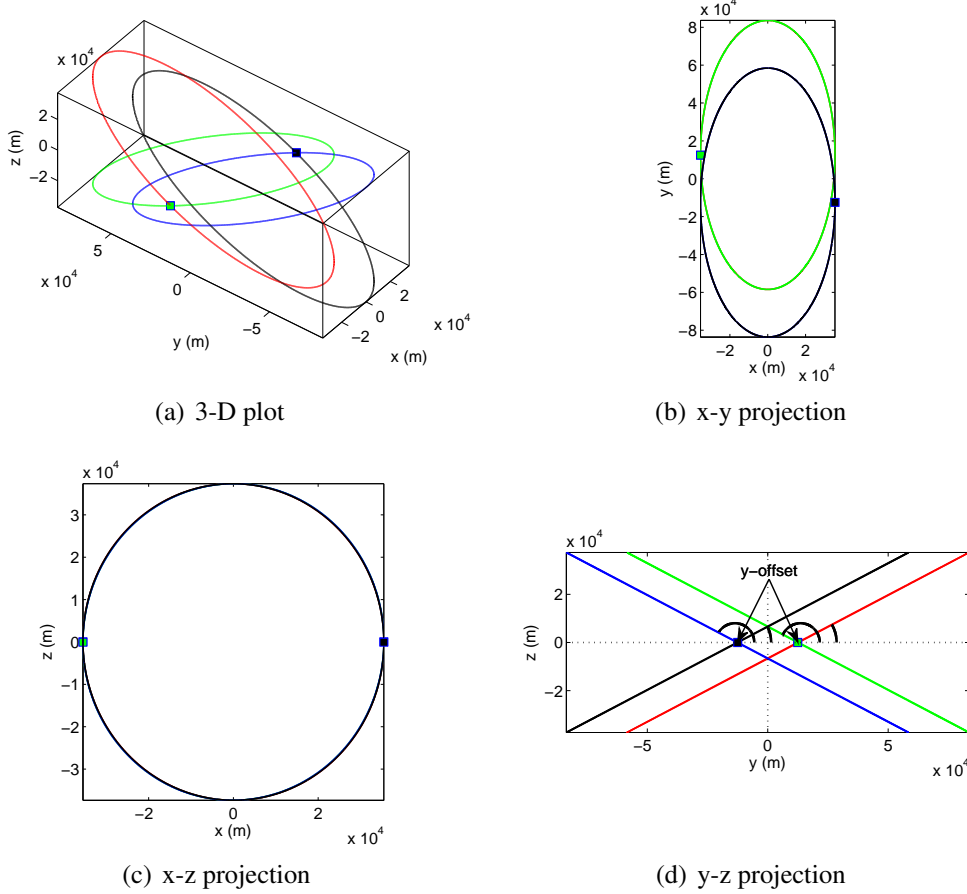


Figure 14. True Relative Orbit and Three Mirror Ambiguous Orbits

6.3 Deformed Ambiguous Orbits

Unlike a mirror ambiguous orbit, a deformed ambiguous orbit implies that the in-plane and out-of-plane motion have different amplitudes than those of the true relative orbit, or $|a'_e| \neq |a_e|$ and $|z'_m| \neq |z_m|$ because Eqs. (32-37) imply that a mismatch of the ambiguous orbit's in-plane and out-of-plane motion magnitude with those of the true relative orbit must occur simultaneously. For a drifting relative orbit, from Eq. (40), we see that $|x_d| = |x'_d|$. From Eqs. (37) and (38), we have $\beta_0 = \beta'_0$, $|a_e x_d| = |a'_e x'_d|$ and $|a_e| = |a'_e|$. Then considering Eqs (32-36), it is easy to find that $|z_m| = |z'_m|$ and $|y_{d0}| = |y'_{d0}|$. In fact, merely by $|a_e| = |a'_e|$ and $|z_m| = |z'_m|$, the existence of a deformed ambiguous orbit for the drifting case is excluded.

Without loss of generality, let us assume $a'_e y'_{d0} = a_e y_{d0}$ from Eq. (41). Furthermore, assume the ratio of in-plane scale of the deformed ambiguous orbit to the true orbit is k , namely,

$$a'_e = k a_e \quad (52)$$

$$y'_{d0} = \frac{1}{k} y_{d0} \quad (53)$$

Thus, from Eqs. (35) and (36) we have

$$\beta'_0 = \beta_0 \quad , \quad \text{for } \beta \in [0, 2\pi) \quad (54)$$

Substituting Eqs. (52-53) into Eqs. (33) and (34), we have

$$4z_m'^2 \cos(2\psi'_0) = 3(k^2 - 1)a_e^2 \cos(2\beta) + 4z_m^2 \cos(2\beta) \quad (55)$$

$$4z_m'^2 \sin(2\psi'_0) = 3(k^2 - 1)a_e^2 \sin(2\beta) + 4z_m^2 \sin(2\beta) \quad (56)$$

Squaring both sides of Eqs. (55) and (56), adding them together and extracting the square root results in

$$4z_m'^2 = \sqrt{9(k^2 - 1)^2 a_e^4 + 16z_m^4 + 24(k^2 - 1)a_e^2 z_m^2 \cos(2\beta_0 - 2\psi_0)} \quad (57)$$

Finally, substituting Eqs. (52-53) and (57) into Eq. (32), we end up with an equation only in terms of k , i.e.,

$$5a_e^2 + 4z_m^2 + 8y_{d0}^2 = 5k^2 a_e^2 + \frac{8}{k^2} y_{d0}^2 + \sqrt{9(k^2 - 1)^2 a_e^4 + 16z_m^4 + 24(k^2 - 1)a_e^2 z_m^2 \cos(2\beta_0 - 2\psi_0)} \quad (58)$$

Defining $K = k^2 > 0$, $C = 5a_e^2 + 4z_m^2 + 8y_{d0}^2$, this can be simplified as

$$C - 5K a_e^2 - \frac{8}{K} y_{d0}^2 = \sqrt{9(K - 1)^2 a_e^4 + 16z_m^4 + 24(K - 1)a_e^2 z_m^2 \cos(2\beta_0 - 2\psi_0)} \quad (59)$$

Squaring both sides of Eq. (59) we obtain

$$\left(C - 5K a_e^2 - \frac{8}{K} y_{d0}^2 \right)^2 = 9(K - 1)^2 a_e^4 + 16z_m^4 + 24(K - 1)a_e^2 z_m^2 \cos(2\beta_0 - 2\psi_0) \quad (60)$$

Finally a fourth order polynomial can be derived as

$$\begin{aligned} & 16a_e^4 K^4 + [18a_e^4 - 24a_e^2 z_m^2 \cos(2\beta_0 - 2\psi_0) - 10C a_e^2] K^3 \\ & + [-9a_e^4 + 24a_e^2 z_m^2 \cos(2\beta_0 - 2\psi_0) + 80a_e^2 y_{d0}^2 - 16z_m^4 + C^2] K^2 - 16C y_{d0}^2 K + 64y_{d0}^4 = 0 \end{aligned} \quad (61)$$

Note that in deriving Eq. (60) from Eq. (59) the solution set of K is increased by “squaring” both sides of Eq. (60). We return to this issue later when we discuss the existence of solutions for K . For now, it is obvious that Eq. (61) is a quartic equation and admits four roots. However, not all the roots are valid, because a valid K for deformed ambiguous orbits must satisfy the following conditions.

$$K > 0 \quad (62)$$

$$K \neq 1 \quad (63)$$

In order to check the solution set of Eq. (61), we test it with a numerical example with initial conditions illustrated in Table 5. If we transform these initial conditions into ROEs and substitute them into Eq. (61), the resulting fourth order polynomial is given by

$$K^4 - 2.4336K^3 + 1.629K^2 - 0.199K + 0.004 = 0 \quad (64)$$

Eq. (64) has four real and positive solutions

$$\begin{bmatrix} K_1 \\ K_2 \\ K_3 \\ K_4 \end{bmatrix} = \begin{bmatrix} 1.283681667559196 \\ 1.0000000000000000 \\ 0.125488302965344 \\ 0.024439677975557 \end{bmatrix} \quad (65)$$

From the solution set, we discuss the following values separately:

1. $K_2 = 1$, i.e., $k_2 = \pm 1$ denotes the true relative orbit and corresponding mirror ambiguous orbits.

2. $K_3 = 0.125 \dots$, denotes a valid deformed ambiguous orbit. With $K = K_3$ and $k = \pm\sqrt{K_3}$, we obtain the ambiguous ROEs by following Eqs. (52-57) and (32-37). Then transforming these ambiguous ROEs back to initial ambiguous Cartesian coordinates, we simulate the ambiguous orbit using HCW dynamics as shown in Figure 15. From Figures 15(b) and 15(c), we see that the in-plane motion amplitude of the ambiguous orbit is decreased compared to that of the true relative orbit while the out-of-plane motion amplitude of the ambiguous orbit is enlarged to compensate the decreased in-plane amplitude and thus yield an identical range history. From our previous analysis on mirror ambiguous orbits, it is seen that whenever one deformed ambiguous orbit is found, there exist three other orbits “mirrored” to this deformed ambiguous orbit generating the same range history. In other words, one valid $K \neq 1$ implies four deformed ambiguous orbits. Figure 15 illustrates the true relative orbit and these four deformed ambiguous orbits. (In fact, two of these deformed ambiguous orbits are corresponding to the second case $a'_e y'_{d0} = -a_e y_{d0}$ from Eq. (41).)

3. K_1 and K_4 are not valid solutions for an ambiguous orbit and are called fake solutions in this paper. The reason that these two K values are not valid ambiguous solutions, as was mentioned earlier, is that the solution set of K is increased by “squaring” both sides of Eq. (59). To explain this, let us define

$$f = C - 5K a_e^2 - \frac{8}{K} y_{d0}^2 \quad (66)$$

and

$$g = \sqrt{9(K-1)^2 a_e^4 + 16z_m^4 + 24(K-1)a_e^2 z_m^2 \cos(2\beta_0 - 2\psi_0)} \quad (67)$$

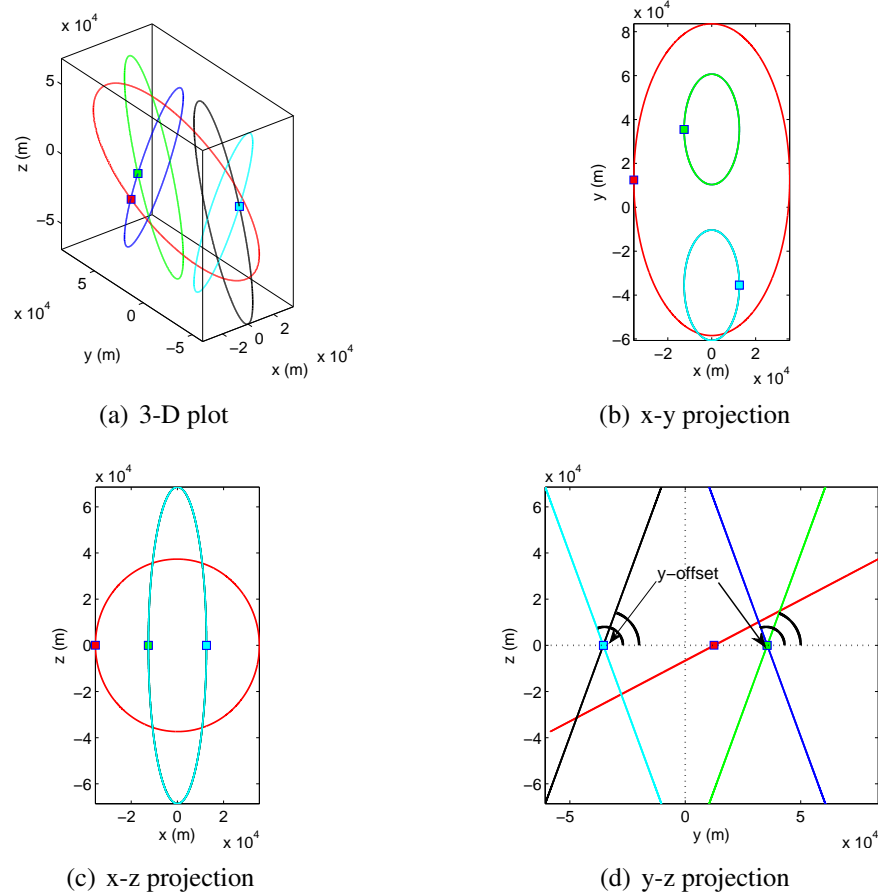


Figure 15. True Relative Orbit and Four Deformed Ambiguous Orbits

Also, we define

$$P_{true} = f - g \quad (68)$$

$$P_{fake} = f + g \quad (69)$$

$$P_{com} = K^2(f^2 - g^2) \quad (70)$$

It is easy to see that $P_{true} = 0$ is equivalent to Eq. (59), $P_{fake} = 0$ is the surplus or “fake” polynomial equation generated by the squaring operation, and $P_{com} = 0$ is equivalent to Eq. (61). Figure 16 illustrates these three polynomials with respect to K . As expected, P_{fake} has two intersections with P_{com} at the two fake solutions K_1 and K_4 , while P_{true} has an additional two intersections with P_{com} at K_2 and K_3 . In other words, both $P_{fake} = 0$ and $P_{true} = 0$ contribute two roots each to $P_{com} = 0$ and only the roots from $P_{true} = 0$ are physically valid for our problem. With these considerations, it is clear that there are at most two real roots of physical interest and one of them is $K = 1$. Therefore, we can conclude that for any closed relative orbit, there exists at most one valid $K \neq 1$ representing deformed ambiguous orbits.

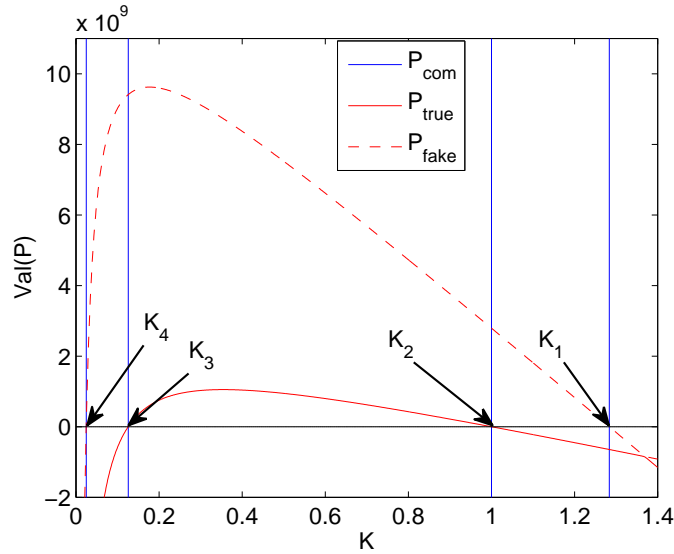


Figure 16. Three Polynomials and Corresponding Solutions

6.4 Existence of Deformed Ambiguous Orbits

Recall that the essence of this problem is to decide the existence of a valid $K > 0$, $K \neq 1$ in Eq. (59). From the previous analysis, we know that this equation has two solutions (because $P_{com} = 0$ has four solutions in total in the context of complex solution). Now we discuss the existence of this ambiguous K . For convenience, define a function $h(K)$ as

$$h(K) = 5K a_e^2 + \frac{8}{K} y_{a0}^2 + \sqrt{9(K-1)^2 a_e^4 + 16z_m^4 + 24(K-1)a_e^2 z_m^2 \cos(2\beta_0 - 2\psi_0)} \quad (71)$$

Therefore, Eq. (59) is equivalent to “ $h(K) = C$ ”. It is obvious that $h(K)$ has the following properties:

1. $h(K) = C$ has two solutions in the complex space.
2. $h(K)$ is a continuous function for $K \in (0, \infty)$.
3. $K = 1$ is one solution for $h(K) = C$.
4. $h(K) \rightarrow \infty$ as $K \rightarrow 0$.
5. $h(K) \rightarrow \infty$ as $K \rightarrow \infty$.

With these five properties, we can qualitatively plot $h(K)$ as Figure 17. From these sub-figures, if $h(K)$ transversely crosses C as shown in Figures 17(a) and 17(b), then we can guarantee $h(K) = C$ has one deformed ambiguous solution at $K = K'$. However, it is possible that $h(K)$ is tangent to C at $K = 1$ as shown in Figure 17(c) where $K = 1$ is a double root and thus no deformed ambiguous K exists. Therefore, we need to discuss the

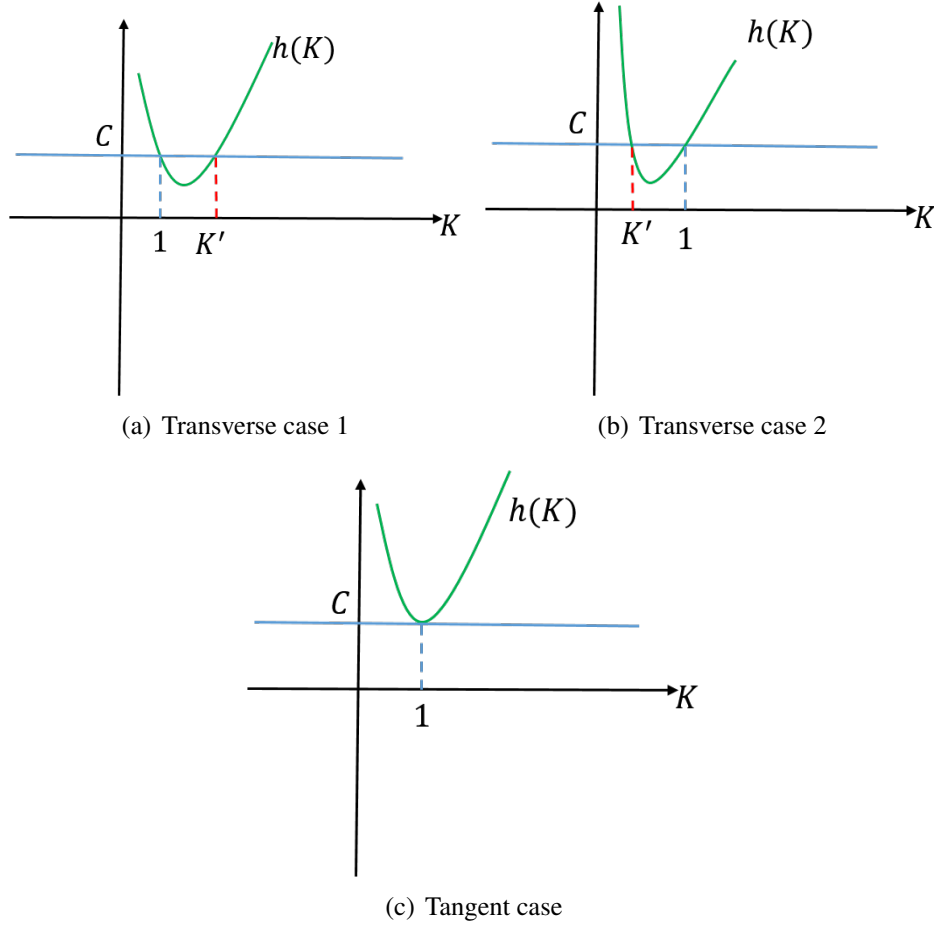


Figure 17. Cases of Transverse and Tangent Intersections for $h(K)$ and C

condition for the tangent case. If $h(K)$ is tangent to C at $K = 1$, it simply means that the derivative of $h(K)$ at the tangent point equals to 0, i.e.,

$$\left. \frac{dh}{dK} \right|_{K=1} = \frac{5}{4}a_e^2 - 2y_{d0}^2 + \frac{3}{4}a_e^2 \cos(2\beta_0 - 2\psi_0) = 0 \quad (72)$$

Note that the condition is independent of z_m . To test the condition for no deformed ambiguous orbits in Eq. (72), we set

$$y_{d0} = \frac{a_e}{2} \sqrt{\frac{5}{2} + \frac{3}{2} \cos(2\beta_0 - 2\psi_0)} = 3.551 \times 10^4 \text{m} \quad (73)$$

in the numerical simulation while keeping the remaining ROEs the same as before in Table 5. With these initial conditions, the quartic equation for K is

$$K^4 - 3.527K^3 + 4.303K^2 - 2.027K + 0.250 = 0 \quad (74)$$

Eq. (74) has four real and positive solutions

$$\begin{bmatrix} K_1 \\ K_2 \\ K_3 \\ K_4 \end{bmatrix} = \begin{bmatrix} 1.340247349090013 \\ 1.000000010460630 \\ 0.999999989539370 \\ 0.186546575287586 \end{bmatrix} \quad (75)$$

It is easy to see that $K_2 \approx K_3 \approx 1$ is the repeated root. The same conclusion can also be drawn from Figure 18.

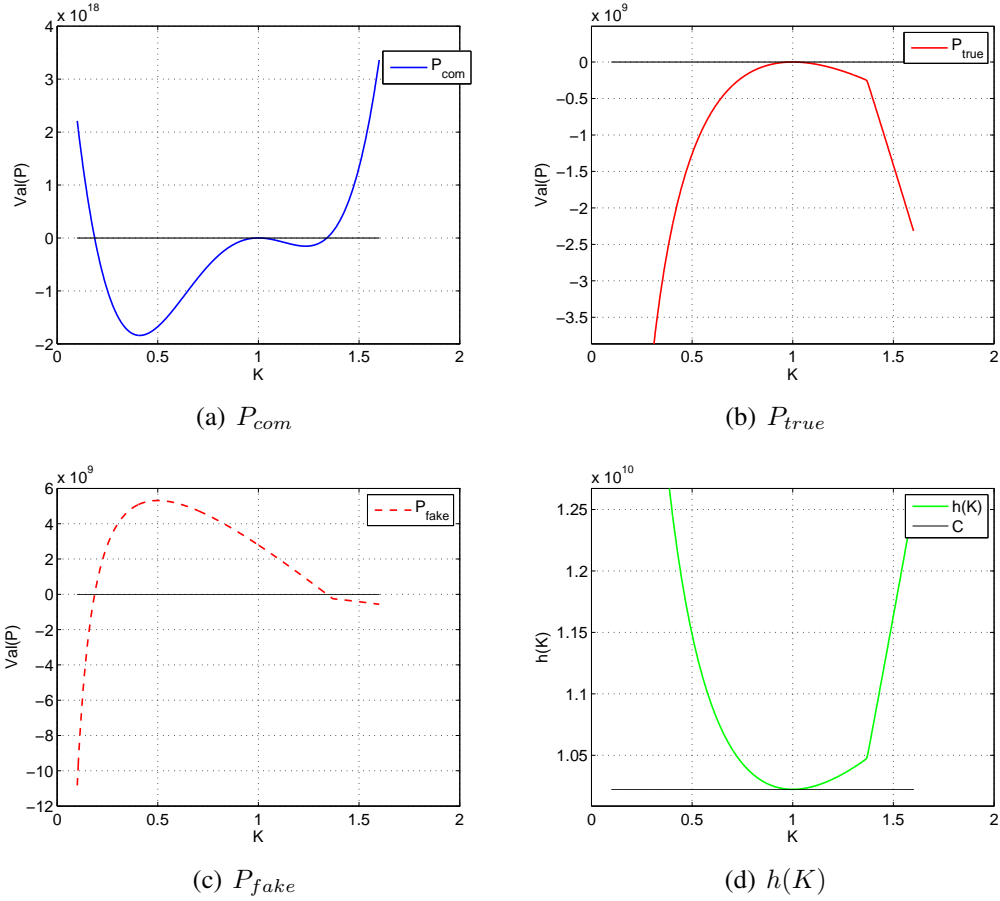


Figure 18. Illustration of Tangent Condition

6.5 Categorization of Ambiguous Relative Orbits

As discussed earlier, we can categorize the ambiguous orbits in terms of initial Cartesian coordinates. However, this criterion is not convenient when categorizing the various types of ambiguous orbits. Therefore, this paper adopts the y - z plane projection to distinguish these orbits. Two parameters pertaining to the y - z projection are used:

1. y_{d0} , the offset in y direction.

2. s , the slope of the semi-major axis of the projected ellipse in the y - z plane as shown in Figure 19. With the non-drifting solution, it can be shown that

$$s = \frac{a_e^2 - z_m^2 - \sqrt{a_4^4 - 2a_e^2 z_m^2 + z_m^4 + 4a_e^2 z_m^2 \sin^2(\beta_0 - \psi_0)}}{2a_e z_m \sin(\beta_0 - \psi_0)} \quad (76)$$

The categorization of the various types of ambiguous orbits in terms of y_{d0} and s is shown in Table 6 with correlation between Cartesian initial coordinates and y - z projection. Also note that we require $\text{sign}(\tilde{y}_{d0}) = \text{sign}(y_{d0})$ and $\text{sign}(\tilde{s}) = \text{sign}(s)$ to decide the primary deformed ambiguous type (d), where $(\tilde{})$ denotes deformed values.

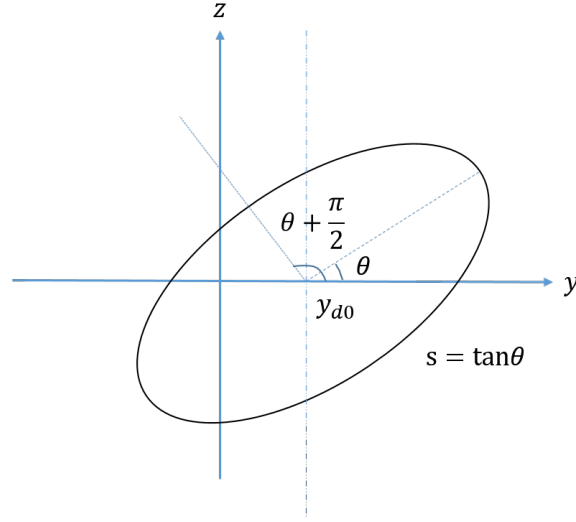


Figure 19. Illustration of Offset y_{d0} and Slope s in y - z Projection

Table 6. Categorization of Ambiguous Orbits

Types	Cartesian coords.	y - z projection	
(t)	$(x_0, y_0, z_0, \dot{x}_0, \dot{y}_0, \dot{z}_0)$	y_{d0}	s
(a)	$(x_0, y_0, -z_0, \dot{x}_0, \dot{y}_0, -\dot{z}_0)$	y_{d0}	$-s$
(b)	$(-x_0, -y_0, z_0, -\dot{x}_0, -\dot{y}_0, \dot{z}_0)$	$-y_{d0}$	$-s$
(c)	$-(x_0, y_0, z_0, \dot{x}_0, \dot{y}_0, \dot{z}_0)$	$-y_{d0}$	s
(d)	$(\tilde{x}_0, \tilde{y}_0, \tilde{z}_0, \tilde{\dot{x}}_0, \tilde{\dot{y}}_0, \tilde{\dot{z}}_0)$	\tilde{y}_{d0}	\tilde{s}
(e)	$(\tilde{x}_0, \tilde{y}_0, -\tilde{z}_0, \tilde{\dot{x}}_0, \tilde{\dot{y}}_0, -\tilde{\dot{z}}_0)$	\tilde{y}_{d0}	$-\tilde{s}$
(f)	$(-\tilde{x}_0, -\tilde{y}_0, \tilde{z}_0, -\tilde{\dot{x}}_0, -\tilde{\dot{y}}_0, \tilde{\dot{z}}_0)$	$-\tilde{y}_{d0}$	$-\tilde{s}$
(g)	$-(\tilde{x}_0, \tilde{y}_0, \tilde{z}_0, \tilde{\dot{x}}_0, \tilde{\dot{y}}_0, \tilde{\dot{z}}_0)$	$-\tilde{y}_{d0}$	\tilde{s}

6.6 Numerical Results for Ambiguity Analysis

In the following discussion, we show numerical examples of convergence of a sequential filter to ambiguous relative orbits by applying drifting mirror, non-drifting mirror and deformed ambiguous initial conditions to an EKF with HCW dynamics. For both drifting and non-drifting examples, the chief orbit is chosen as a circular orbit with a radius of 7100 km, and the orbital element differences are shown in Table 7.

The measurement covariance matrix is assumed to be $R = 20^2 \text{ m}^2$ and the sample time is $\Delta t = 10$ seconds. The initial states guess for the EKF is $\bar{\mathbf{X}}_0 = (\bar{x}_0, \bar{y}_0, \bar{z}_0, \bar{\dot{x}}_0, \bar{\dot{y}}_0, \bar{\dot{z}}_0)^T = (x'_0, y'_0, z'_0, \dot{x}'_0, \dot{y}'_0, \dot{z}'_0)^T$, where $i = (t), (a), \dots, (f)$ in Table 6, and the true initial condition $\mathbf{X}_0 = (x_0, y_0, z_0, \dot{x}_0, \dot{y}_0, \dot{z}_0)^T$ is calculated from orbital element differences in Table 7. We note that the range measurements were generated from integrating nonlinear two-body equations of motion, so that the range history does not exactly match that generated from HCW dynamics. Figure 20 illustrates the drifting estimated orbits with type (t), type (a), type (b) and type (c) initial conditions, in which the red line denotes the true relative orbit and blue line denotes estimated orbits.

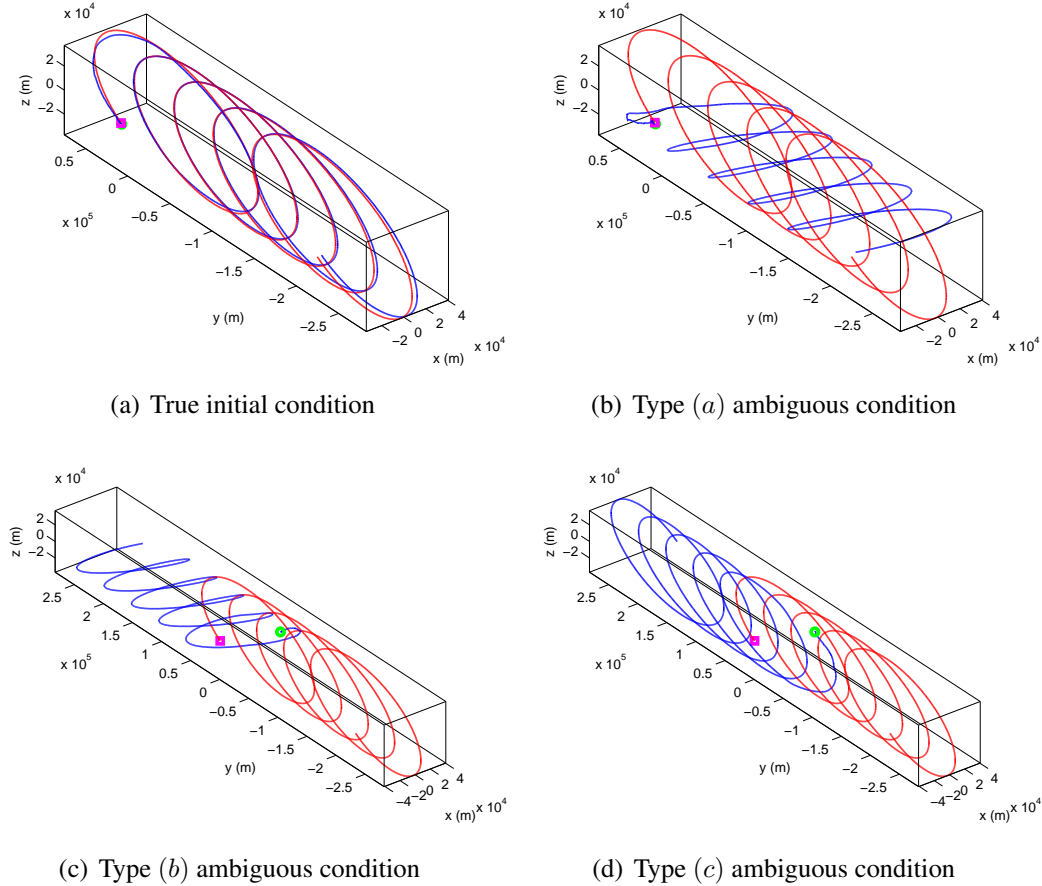


Figure 20. Drifting True and Mirror Ambiguous Orbits in an EKF Simulation

Figure 20(b) shows the inversion of the z -motion for type (a) orbit, Figure 20(c) shows the inversion of the xy -motion for type (b) orbit, and Figure 20(d) shows the inversion of the xyz -motion for type (c) orbit. From these figures, it is clear that the filter can still arrive at ambiguous orbits despite the fact that their range history is different than that of the measurements.

Table 7. Orbital Element Differences for Drifting and Non-drifting Scenarios

	δa	δe	δi	$\delta \Omega$	$\delta \omega$	δM_0
Drifting	5 km	0.005	0.3°	0°	0°	0.1°
Non-drifting	0 km	0.005	0.3°	0°	0°	0.1°

For the closed orbit, Figure 21 shows the results of applying the type (c) mirror ambiguous condition in the EKF. From the numerical results, the filter reproduces the type (c) mirror ambiguous orbit except with a small disturbance at the beginning because of the mismatch in measurement model (full nonlinear) and filter dynamic model (HCW), process noise and measurement noise. It is worthy to mention that we also found cases where the EKF filter converged to smooth mirror ambiguous orbits of type (a) and (b).

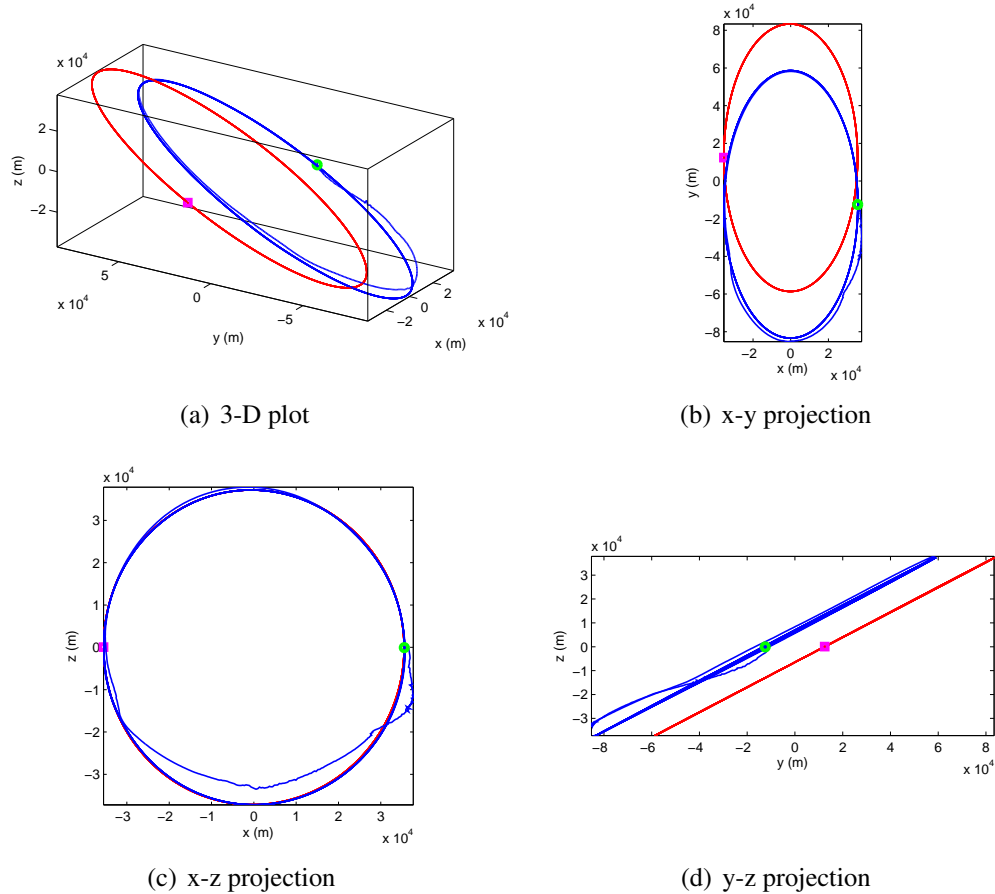


Figure 21. Type (c) Mirror Ambiguous Orbit in an EKF Simulation

Also, in order to check whether the filter will converge to a deformed ambiguous orbit, we applied the type (e) ambiguous initial condition to an EKF. Figure 22 illustrates the corresponding results. From these plots, the estimated orbit does converge to the “pre-designed” deformed ambiguous orbit after a certain initial oscillation.

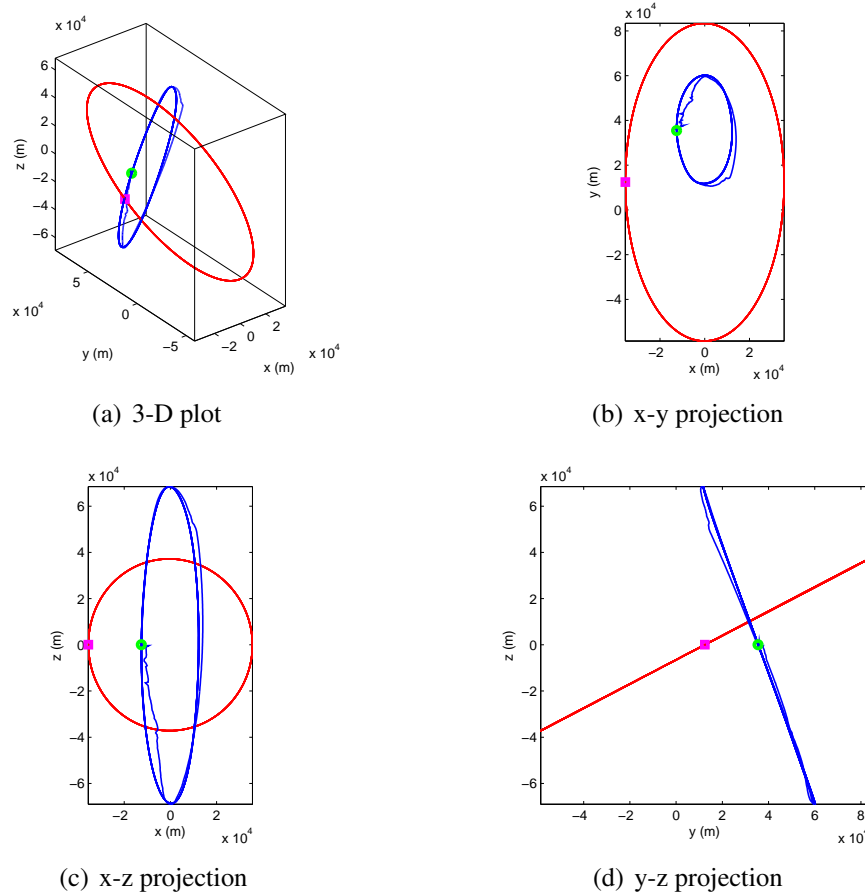


Figure 22. Type (e) Deformed Ambiguous Orbit in an EKF Simulation

Some general results on the increased observability obtained by using higher order nonlinearities in the EKF resulting from the Taylor expansion about the chief orbit have been shown. Therefore, we conduct a comprehensive set of numerical simulations to illustrate the ability of quadratic, cubic and full two-body nonlinearities in the filter model to avoid or resist the occurrence of ambiguous orbits for range-only measurements. We consider the effects of varying three independent characteristics:

1. Nonlinear order of dynamic model used in the EKF. Again four different dynamic models (first, second, third order and full nonlinear dynamic models) are applied in the EKF as defined earlier.

- Size of the relative orbit. Since the accuracy of describing relative motion using a lower order dynamic model decreases as the relative separation is enlarged, three configuration scenarios are taken into account as shown in Table 8, where ρ_{avg} is the average relative range over the course of one orbit period.

Table 8. Orbital element Differences for Three Simulation Scenarios

relative orbit size	δa	$\delta \Omega$	$\delta \omega$	δe	δi	δM_0	ρ_{avg}
small	0	0	0	0.005	0.3°	0.1°	60 km
medium	0	0	0	0.025	1.5°	0.5°	300 km
large	0	0	0	0.05	3°	1°	600 km

- Geometric variation of the initial guess given to the EKF. In order to keep the shape and size of the relative orbit unchanged for one set of variations, we alter the initial guess for the EKF geometrically using ROEs. To achieve this purpose, a_e and z_m must remain constant and y_{d0} , β_0 , and ψ_0 are manipulated to fulfill the variation of initial condition. For example, from Eq. (51) and Eq. (76), varying from type (t) to type (c) mirror ambiguous orbit, we need to keep the phase difference $\beta_0 - \psi_0$ constant for slope. Meanwhile, to reverse the sign of in-plane and out-of-plane motion, we need to vary the phase angles from $[\beta_0, \psi_0]$ to $[\beta_0 + \pi, \psi_0 + \pi]$ and offset in y direction from y_{d0} to $-y_{d0}$. Numerically, the initial guess in the EKF is set as $[\bar{\beta}_0, \bar{\psi}_0, \bar{y}_{d0}] = [\beta_0, \psi_0, y_{d0}] + \gamma[\pi, \pi, -2y_{d0}]$, where γ is the variation coefficient with increment of 0.01. The variation strategy is shown in Figure 23 with the 3D view and y - z projection.

The results of this comprehensive numerical investigation are shown and discussed in the following section.

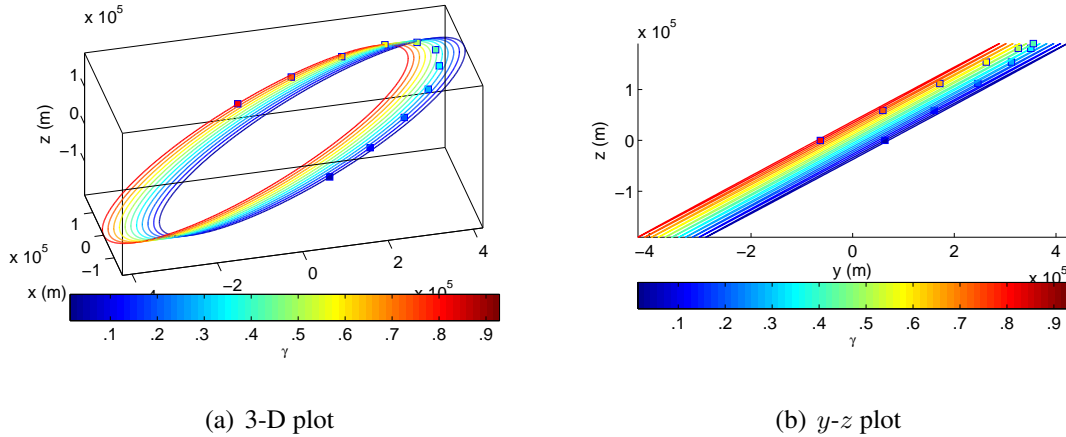


Figure 23. Relative Orbits Resulting from Variation of Initial Conditions

7.0 RESULTS AND DISCUSSION

The first set of simulations explores the variation from type (t) to type (c) mirror ambiguous orbit for the small relative orbit scenario. The numerical results are shown in Figure 24, which is called a “step plot” and in which the horizontal lines indicate convergence and the slant lines denote non-convergence. (Note the filter is regarded as converged to type (i) orbit if the resulting y_{d0} and s of the estimated orbit are within 90% of those of type (i)). From this figure, it is seen that the filter with HCW dynamic model diverges earliest at $\gamma = .26$, the second order model diverges next at $\gamma = .33$ and lastly the third order and full nonlinear models at $\gamma \approx .53$. This means that higher order dynamic models have larger basins of attraction to the true orbit compared with lower order dynamic models, which converge more easily to ambiguous orbits.

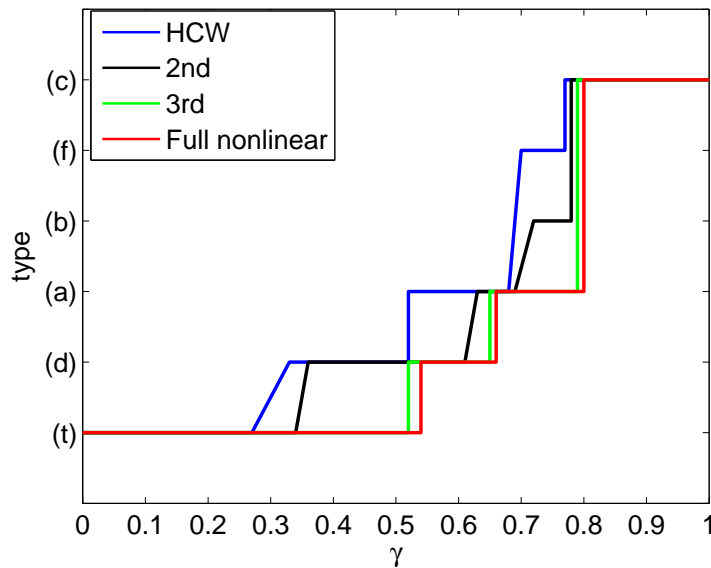


Figure 24. Convergence of EKF Simulations for Small Relative Orbit Scenario

Another interesting observation from Figure 24 is that instead of only converging to type (t) and (c) orbits, which are the endpoints of the variation, the filter also converges to type (d), (a), (b) and (f) ambiguous orbits. The value of γ where the EKF switches from convergence to one ambiguous orbit to convergence to the "next" ambiguous orbit, increases for higher order nonlinear models. In other words, the use of higher order nonlinear models tend to delay or resist the appearance of ambiguous orbits in the EKF.

The step plots for the medium and large scenarios are shown in Figure 25. Figure 25(a) and 25(b) are very similar to Figure 24 in terms of the resistance of the higher order nonlinear models to ambiguous orbits except that for each order model, the range of γ over which the EKF converges to a particular ambiguous relative orbit has changed. To observe more carefully the effects of large separation, Figures 26 and 27 show the step plots for the HCW and full nonlinear models with medium and large configuration scenarios.

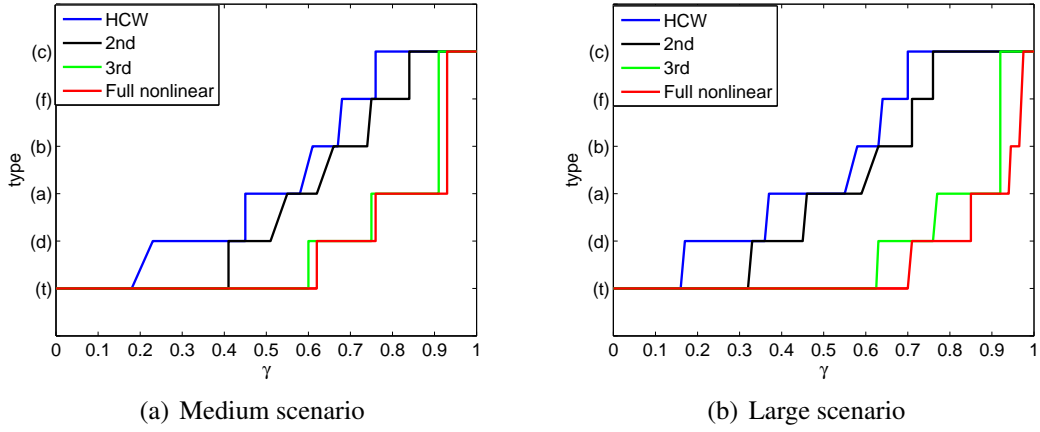


Figure 25. Convergence of EKF for Medium and Large Relative Orbit Scenarios

From Figure 26, for the HCW dynamic model, the divergence from the true orbit becomes faster when switching from small to medium, and also from medium to large relative orbit scenarios. This result agrees with our expectation because the range profile in the EKF is generated by the full nonlinear dynamic model and the HCW model has less ability to track the real motion and real range.

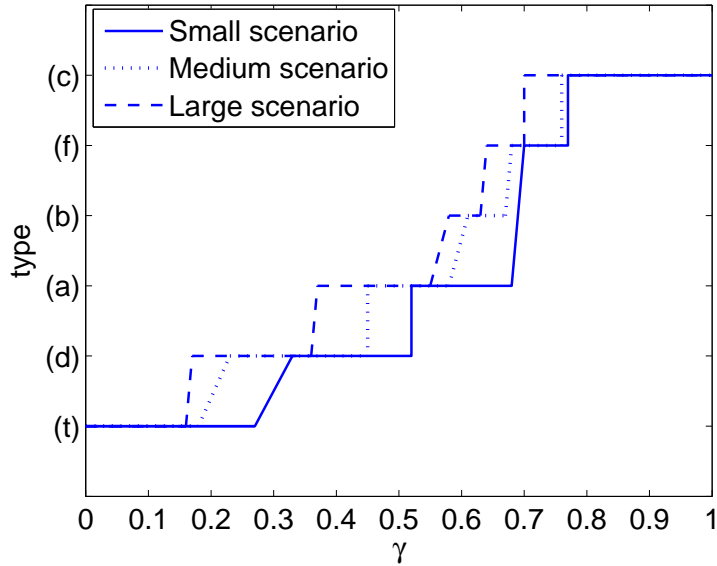


Figure 26. Convergence of EKF for HCW Model with Three Relative Orbit Scenarios

On the contrary, Figure 27 shows that the filter diverges later when switching from smaller to larger separation scenarios for the full nonlinear model. The reason is that even though the ambiguous orbits perfectly exist for HCW dynamics, they are not exactly suitable for the higher order or full nonlinear dynamics. In other words, a full nonlinear model

can never generate the exact same range history of the true orbit from a different orbit for which there always exist errors in range. Therefore, the full nonlinear model can utilize this mismatch in range to distinguish and discard the ambiguous orbit. The same conclusion could also be drawn by performing the same analysis with the second and third order models in the EKF. Results would look similar to the plots in Figures 26 and 27.

In total, the use of higher order nonlinear models in the EKF can resist the tendency to converge to an ambiguous orbit. This resistive effect becomes more obvious when the relative separation of the formation configuration is enlarged. It is noted that we also studied other directions of variation such as $(t) \rightarrow (f)$, $(t) \rightarrow (a)$ and $(t) \rightarrow (b)$, and this conclusion holds for these variations as well.

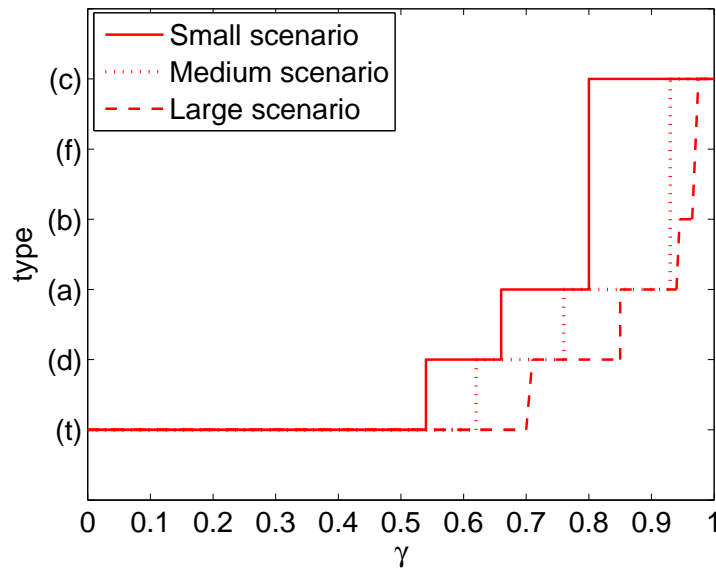


Figure 27. Convergence of EKF for Full Nonlinear Model with Three Scenarios

8.0 CONCLUSIONS

In this report, the observability of relative orbit estimation for circular chief orbits with different orders of nonlinearities in the filter model was studied. Using the Lie derivative method, analytical observability conditions were obtained for relative orbit models with different orders of nonlinearities. The benefits of using higher order dynamic models were manifested both by the Lie derivative method and by the numerical analysis using quantitative measures of observability obtained from the observability Gramian, covariance matrix, and estimation error RMS.

To explain the reason for the appearance of ambiguous orbits in a Hill-Clohessy-Wiltshire based EKF, the ambiguous relative orbits generated from range-only measurements was analyzed both by analytical derivation and numerical simulation. Two categories of ambiguous orbits were shown to exist: mirror ambiguous orbits and deformed ambiguous orbits, and conclusions were drawn regarding the types and numbers of ambiguous orbits. Specifically, it is shown that: 1) For non-drifting relative orbits, three mirror ambiguous orbits and four deformed ambiguous orbits exist. The deformed ambiguous orbits disappear when the tangent condition is satisfied. 2) For drifting relative orbits, only three mirror ambiguous orbits exist. These facts are a consequence of the global unobservability of an estimation strategy based on range-only measurements and HCW dynamics. Also when used as a dynamic model in a filter the higher order nonlinear models of relative motion were shown to have the potential to resist the tendency of an extended Kalman filter to converge to an ambiguous relative orbit, particularly for large separation relative orbits.

REFERENCES

- [1] P. J. Huxel and R. H. Bishop, "Navigation algorithms and observability analysis for formation flying missions," *Journal of Guidance, Control, and Dynamics*, Vol. 32, No. 4, 2009, pp. 1218–1231.
- [2] J. R. Yim, J. L. Crassidis, and J. L. Junkins, "Autonomous orbit navigation of two spacecraft system using relative line of sight vector measurements," *Proc. AAS Astrodynamics Specialist Conf., Maui, HI, Paper No. 04-257*, Vol. 13, No. 4, Feb. 8-12, 2004.
- [3] D. C. Woffinden and D. K. Geller, "Observability criteria for angles-only navigation," *IEEE Transactions on Aerospace and Electronic Systems*, Vol. 45, No. 3, 2009, pp. 1194–1208.
- [4] D. C. Woffinden and D. K. Geller, "Optimal orbital rendezvous maneuvering for angles-only navigation," *Journal of Guidance, Control, and Dynamics*, Vol. 32, No. 4, 2009, pp. 1382–1387.
- [5] W. H. Clohessy and R. S. Wiltshire, "Terminal guidance system for satellite rendezvous," *Journal of the Aerospace Sciences*, Vol. 27, No. 9, 1960, pp. 653–658.
- [6] G. W. Hill, "Researches in the lunar theory," *American Journal of Mathematics*, Vol. 1, No. 1, 1878, pp. 5–26.
- [7] E. Kaufman, A. T. Lovell, and T. Lee, "Nonlinear observability measure for relative orbit determination with angles-only measurements," *Proc. AAS Astrodynamics Specialist Conf., Williamsburg, VA, Paper No. 23-451*, Jan 11-15, 2015.
- [8] M. L. Psiaki, "Autonomous orbit determination for two spacecraft from relative position measurements," *Journal of Guidance, Control, and Dynamics*, Vol. 22, No. 2, 1999, pp. 305–312.
- [9] C. Rundberg and T. Lovell, "Relative Spacecraft Navigation via Inter-Satellite Range Measurements," *AAS Guidance and Control Conference, Breckenridge, CO, Paper No. 16-016*, Feb 5-10, 2016.
- [10] K. Alfriend, S. R. Vadali, P. Gurfil, J. How, and L. Breger, *Spacecraft Formation Flying: Dynamics, Control and Navigation*, Vol. 2. Butterworth-Heinemann, 2009.
- [11] D. Richardson and J. Mitchell, "A third-order analytical solution for relative motion with a circular reference orbit," *The Journal of the Astronautical Sciences*, Vol. 51, No. 1, 2003, pp. 1–12.
- [12] S. R. Kou, D. L. Elliott, and T. J. Tarn, "Observability of nonlinear systems," *Information and Control*, Vol. 22, No. 1, 1973, pp. 89–99.
- [13] E. W. Griffith and K. Kumar, "On the observability of nonlinear systems: I," *Journal of Mathematical Analysis and Applications*, Vol. 35, No. 1, 1971, pp. 135–147.
- [14] A. J. Krener and K. Ide, "Measures of unobservability," *Decision and Control, 2009 held jointly with the 2009 28th Chinese Control Conference. CDC/CCC 2009. Proceedings of the 48th IEEE Conference on, IEEE, Shanghai, China*, 2009, pp. 6401–6406.
- [15] W. Waldraff, D. Dochain, S. Bourrel, and A. Magnus, "On the use of observability measures for sensor location in tubular reactor," *Journal of Process Control*, Vol. 8, No. 5, 1998, pp. 497–505.
- [16] D. Dochain, N. Tali-Maamar, and J. Babary, "On modelling, monitoring and control of fixed bed bioreactors," *Computers & Chemical Engineering*, Vol. 21, No. 11, 1997, pp. 1255–1266.
- [17] T. A. Lovell and S. G. Tragesser, "Guidance for relative motion of low earth orbit spacecraft based on relative orbit elements," *Proc. AAS Astrodynamics Specialist Conf., Providence, RI, Paper No. 4998*, Aug 16-19, 2004.

LIST OF SYMBOLS, ABBREVIATIONS, AND ACRONYMS

HCW	Hill-Clohessy-Wiltshire
LVLH	Local Vertical Local Horizontal
EKF	Extended Kalman Filter
OI	Observability Index
CN	Estimation Condition Number
RMS	Root Mean Square
ROE	Relative Orbital Elements

Symbol	Description
μ	Gravitational Parameter of the Earth
n	Mean Motion of Chief Orbit
r_c	Orbital Radius of Chief Orbit
ω	Angular Velocity of Chief Orbit
\mathbf{v}_c	Velocity of Chief Spacecraft
x, y, z	Cartesian Position Coordinates in Chief's LVLH Frame
$\dot{x}, \dot{y}, \dot{z}$	Cartesian Velocity Coordinates in Chief's LVLH Frame
ρ	Range Vector From Chief to Deputy
\mathbf{X}	Deputy's Position and Velocity
\mathbf{r}_d	Position of Deputy Spacecraft Relative to Center of the Earth
\mathbf{F}_i	Vector field of i th Order Dynamic Model of Relative Motion
Γ_i	i th Order Nonlinear Terms
\mathbf{v}_{rel}	Velocity of Deputy Relative to the Chief
λ	In-plane Bearing Angle
ϕ	Out-of-plane Bearing Angle
W_c	Gramian for Continuous System
W_d	Gramian for Discrete System
Φ	State Transition Matrix
H	Jacobian Matrix of the Output Relation
σ	Singular Value of a Matrix
a	Semi-major Axis of an Orbit
e	Eccentricity of an Orbit
i	Inclination of an Orbit
Ω	Argument of Ascending Node of an Orbit
ω	Argument of Periapsis of an Orbit
M_0	Initial Mean Anomaly of an Orbit
P_0	Initial Covariance Matrix
R	Measurement Covariance Matrix
Δt	Sampling Time Interval
e_ρ	Estimation Position Error
\dot{e}_ρ	Estimation Velocity Error
a_e	Magnitude of In-plane Motion
z_m	Magnitude of Out-of-plane Motion
x_d	Offset in x Direction
y_d	Offset in y Direction
β	In-plane Phase Angle
ψ	Out-of-plane Phase Angle
s	Slope of the Semi-major Axis of the Projected Ellipse in y - z Plane
γ	Geometric Variation Coefficient

DISTRIBUTION LIST

DTIC/OCF	
8725 John J. Kingman Rd, Suite 0944	
Ft Belvoir, VA 22060-6218	1 cy
AFRL/RVIL	
Kirtland AFB, NM 87117-5776	2 cys
Official Record Copy	
AFRL/RVSV/Thomas Lovell	1 cy

Approved for public release; distribution is unlimited.

(This page intentionally left blank)